Synopsis of PhD Thesis

Physics of Jets from the Comprehensive Timing Analyses of the Emission Variability of Blazars

By

Susmita Das

Registration No.: R-18RS209220248

Supervisor: Dr. Ritaban Chatterjee

PRESIDENCY UNIVERSITY
KOLKATA

School of Astrophysics
Presidency University
Kolkata, India

2025

Declaration

I hereby declare that this thesis entitled ***"Physics of Jets from the Comprehensive Timing Analyses of the Emission Variability of Blazars"*** contains original research work carried out by me under the guidance of **Dr. Ritaban Chatterjee**, Assistant Professor at the School of Astrophysics, Presidency University, Kolkata, India to be submitted for the degree of Doctor of Philosophy.

I also declare that, as required by these rules and conduct, I have fully cited and referenced all materials and results that are not original to this work.

I also declare that, this work has not been submitted for any degree either in part or in full to any other institute or university before.

Signature of Candidate: Sreemita Das

Date: 10-02-25

Forwarded by the Supervisor: Ritaban Chatterjee

Assistant Professor
School of Astrophysics
Presidency University, Kolkata

Abstract

Powerful collimated outflows or jets are observed in various astronomical sources including Galactic X-ray binaries, supernova remnants, and young stellar objects as well as extragalactic sources such as gamma-ray bursts and active galactic nuclei (AGN). Studying jets is crucial to understand the exotic physics of these objects, e.g. accretion on to black holes, acceleration of particles to very high ($\sim$TeV) energies within a few hours as well as the influence of jets on its surrounding medium, which affects galaxy formation and evolution. Blazars are a class of AGN, in which the jet is closely aligned to our line of sight and the relativistically beamed emission from the jet dominates the blazar spectral energy distribution, making them ideal sources to observationally probe the jet phenomena. High-amplitude variability of emission, within a time span of minutes to years, is one of the defining properties of blazars. This characteristic is useful to probe the physical properties and emission mechanisms in the jet. Using AstroSat and (quasi)simultaneous multi-wavelength observations, we explore the short-timescale (minutes to days) variability of blazars. We select X-ray-bright blazars, e.g., Mrk 421 and 1ES 1959+650, such that short-timescale variability may be studied with sufficiently high signal to noise ratio.

From multi-wavelength observations of Mrk 421, we find its shortest variability timescale $\sim$ 1.1 ks at the hard X-ray energies and increasingly longer at soft X-rays, optical and near infrared wavelengths. By assuming synchrotron cooling responsible for the fastest variability, we estimate the value of the magnetic field 0.5 Gauss and the maximum Lorentz factor of the emitting electrons $\sim 1.6 \times 10^5$. These results are a confirmation of the leptonic model of blazar emission and in particular the synchrotron origin of the X-ray emission from Mrk 421.

We study the simultaneous soft ($0.7-7$ keV) and hard ($7-20$ keV) X-ray light curves of the above two blazars using SXT and LAXPC instruments onboard the Indian space telescope AstroSat at multiple epochs during 2016-19. We find that the hard and soft X-ray variability are strongly correlated at 95% significant level or higher. The estimated time lag is consistent with zero in some epochs, and indicates hard or soft lag of a few hours in the rest. The soft lag may be due to slower radiative cooling of lower energy electrons while hard lag may be caused by gradual acceleration of the high energy electrons emitting at the hard X-ray band. Assuming the above scenario and the value of the Doppler factor (δ) $10-20$, the hard and soft lags may be used to estimate the magnetic field ~ 0.1 Gauss and the acceleration parameter $\sim 10^4$ in the emission region. The latter provides useful constraints on the theories of particle acceleration in blazar jets.

We analyse the $0.7-20$ keV X-ray spectra of those two blazars at the above epochs. The spectra are fitted by log-parabola model satisfactorily. We carry out time-resolved X-ray spectroscopy in bins of ~ 10 ks at all the above epochs, and study the correlation of the best-fit spectral parameters. We compare those observed results with the spectral variation obtained from a theoretical model of time variable nonthermal emission from blazar jets. It shows that gradual acceleration and radiative cooling of emitting particles belonging to an initial simple power-law energy distribution in presence

of turbulent magnetic field can reproduce most of the observed results. Additional features in the model are required to simulate X-ray emission with more realistic properties in the jets of blazars.

We further study X-ray variability by computing the cross-spectrum, i.e., cross-correlation at the Fourier domain in search of whether there are different temporal properties at different timescales. We perform the analysis for two HSP blazars, namely, 1ES 1959+650 and Mrk 501 using *AstroSat* data at multiple epochs. We get lag-spectra and coherence between the X-ray bands at $0.7-2$ keV, $2-7$ keV and $7-20$ keV energies. It shows that the lower frequency time lag is consistent with the cross-correlation time delay (zero/non-zero) and it become dominated by Poisson noise at higher frequencies. In some cases, time lag makes significant transition from hard to soft or soft to hard with increasing frequency. Then we discuss the results in respect of several physical scenarios i.e., gradual acceleration, synchrotron cooling, and small-amplitude fluctuations in the magnetic field that affect the flux variability at different timescales.

Contents

1 Introduction **5**

1.1 Blazars 6

1.2 Radiative Process 7

2 Multi-Wavelength Variability of the Blazar Markarian 421 **8**

2.1 Data Set 8

2.2 Results 9

2.3 Discussion 11

3 Correlated Hard-Soft X-ray Variability of the Blazars Mrk 421 and 1ES 1959+650 **12**

3.1 AstroSat Data 12

3.2 Cross-Correlation Analysis 12

3.3 Discussion 15

4 Sub-Day Timescale X-ray Spectral Variability **18**

4.1 X-ray Data 19

4.2 Spectral Analysis 19

4.3 Theoretical Modeling of Jet Emission 21

4.4 Discussion 27

5 Cross-Spectral Analysis of Hard and Soft X-ray Variations **30**

5.1 Data 30

5.2 Phase Spectrum 32

6 Discussion **32**

7 Summary and Future Work **35**

1. Introduction

Active galactic nuclei (AGN) are the most luminous non-transient astrophysical objects in the Universe. They are located in the central region of a certain class of galaxies and are powered by the accretion of matter on to a central supermassive black hole (SMBH) of mass $10^6 M_\odot$ to $10^{10} M_\odot$ (Salpeter 1964; Zel'dovich & Novikov 1964). Those galaxies are called active galaxies. The accretion occurs through a planar flow, called accretion disk (Shakura & Sunyaev 1973). Surrounding the disk, there are broad and narrow emission line emitting gas in the broad line region (BLR) and narrow line region (NLR), respectively and molecular dusty material in the shape of a torus (see figure 1). In BLR, gas clouds orbit the SMBH with velocity 10^3 to 10^4 kms^{-1} at $\sim 0.1-1$ pc away from the central engine (Gaskell 2009). The dusty torus (DT) is at $\sim 1-10$ pc (Antonucci & Miller 1985), and the NLR, containing gas clouds of speed 10^2-10^3 kms^{-1} (Netzer & Laor 1993), is located $\sim$kpc away from the center. In addition, some AGNs exhibit highly collimated bipolar outflows (Blandford & Rees 1974) of magnetized plasma, termed 'jet', which can extend from pc to hundreds of kpc scale through the interstellar (ISM) and intergalactic medium (IGM). Jets are bright in the radio band due to synchrotron radiation and in some cases they interact with the IGM to produce giant lobes of radio-bright emission. Based on the presence of jets, AGNs are classified into two broad classes, namely, radio-loud and radio-weak (Franceschini et al. 1998). Observations show that $10\%-20\%$ of AGNs are radio-loud type (Kellermann et al. 1989). On the other hand, according to the orientation towards the observer, various substructures of AGNs are more prominently visible to different observers. Radio galaxies, quasars, and blazars are three subclasses of radio-loud AGNs based on their orientation. (Lawrence et al. 1987; Padovani et al. 2017).

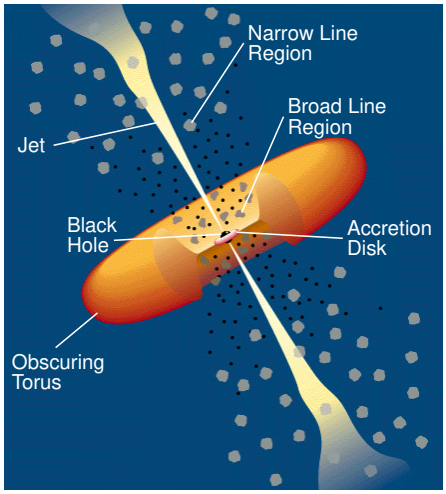

Fig. 1.— Schematic diagram of active galactic nuclei by Urry & Padovani (1995)

1.1. Blazars

Jets are observed not only in AGNs but also in various other astronomical objects, e.g., gamma-ray bursts, X-ray binaries, pulsar powered remnants of supernova explosions, and young stellar objects. The broad spectrum and rapid variability often imply that particles in jets may be accelerated to energies up to a TeV at a few hours timescale. While not all accreting systems produce a detectable jet, in all cosmic systems containing jets, the presence of an accretion disk is inferred from observations. Hence, understanding the launching and collimation of the jets are necessary to comprehend the detailed physics of the accretion process. On the other hand, jets tend to strongly influence their surrounding interstellar and intergalactic medium, thereby affecting galaxy formation and evolution (Richstone et al. 1998; McNamara & Nulsen 2007). Due to relativistic beaming, jets are sometimes observed as very bright point sources and hence may be used as a probe of the distant Universe and the intergalactic medium.

For the above reasons, probing the physics of jets by analyzing its observed properties is an important endeavor in astrophysical studies. Blazars happen to be a very suitable class of sources for studying jets. In blazars, the jet, moving at relativistic speed, is aligned to the observer's line of sight within a small angle $< 10^{\circ}$ (Blandford & Eichler 1987). Due to such orientation, the jet emission is beamed in the observer's reference frame (e.g., Ghisellini et al. 1993). Consequently, the observed luminosity is amplified by a factor δ^4, where the Doppler factor $\delta = \frac{1}{\Gamma(1-\beta\ cos\theta)}$, β is the relativistic speed and θ is the observing angle. As a result, blazar emission is dominated by that from the jet while radiation from other parts of the AGN, e.g., accretion disk, BLR, and the host galaxy are partially or fully overwhelmed by the former.

High-amplitude variability of emission is a characteristic property of blazars which can be used to probe the physics of jets. Due to relativistic beaming blazar emission variability timescale is shortened by a factor of δ in the observer's frame. Consequently, blazars exhibit dramatic variation at all wavelengths and timescales ranging from minutes to decades (Zhang 2002; Chatterjee et al. 2008; Rajput et al. 2020). The nature of the blazar variability is similar to red noise, i.e., longer timescale fluctuations exhibits larger amplitude (Lawrence et al. 1987; Chatterjee et al. 2012). The variability may be due injection of high energy particles by a moving shock wave down the jet originally caused by instabilities in the accretion flow, radiative cooling of emitting particles, turbulence in the jet magnetic field, and change in physical parameters or dominating emission mechanism (Marscher 2016; Böttcher 2019).

Blazars emit at all wavelengths, sometimes radio to high energy γ-rays. The spectral energy distribution (SED) of blazars shows two broad hump-like structures (Abdo et al. 2010; Giommi et al. 2012). One is at the infrared (IR) to ultraviolet (UV)/X-ray wave bands and another arises at the keV to GeV energy range sometimes extending to TeV energies. Flat Spectrum Radio Quasar (FSRQ) are a kind of blazars, which contain prominent emission lines in their spectrum while BL Lac objects show very weak or no emission lines (Ghisellini et al. 2011).

1.2. Radiative Process

The jet plasma in blazars is strongly magnetized. Charged particles are accelerated around the magnetic field lines and emit non-thermal synchrotron radiation, which shows strong polarization (Blinov et al. 2016; Lister et al. 2018; Liodakis et al. 2022). The lower energy peak of the blazar SED is dominated by synchrotron radiation (Bregman et al. 1981; Marscher 1998) by the relativistic electrons in the jet. Regarding the higher energy peak of the SED, there are two different emission models in blazars, namely, leptonic and hadronic, based on the constituent of the jet plasma. In the "leptonic model", only electrons and positrons contribute significantly to the jet emission. In that scenario, inverse-Compton (IC) scattering plays an important role in the higher energy emission, i.e., X-ray to very high energy (VHE) γ-rays. Lower energy 'seed' photons get up-scattered to higher energies by the same relativistic electrons that produces the synchrotron radiation. The seed photons may be from the internal/external sources. When the seed photons are synchrotron photons from the jet itself, it is called synchrotron-self Compton (SSC) (Sikora et al. 1994; Bloom & Marscher 1996) and if those come from outside, e.g., BLR, torus, or accretion disk, it is called external Compton (EC) (Ghisellini et al. 1998; Böttcher & Dermer 2010).

Alternatively, in the hadronic scenario, protons in the jet are accelerated to ultra-relativistic energies and contribute to the higher energy emission via synchrotron process, proton-initiated cascades and the interaction of secondary particles with photons (Mücke et al. 2003; Ackermann et al. 2016). In most cases, leptonic model is sufficient to explain the spectral and variability properties of blazar emission. In a small number of cases hadronic models have been more satisfactory in modeling the higher energy (GeV - TeV) part of the SED of some blazars. However, it requires small size of the emission region (few gravitational radius of the central SMBH), large magnetic field value ($\sim$50 Gauss) and proton energy up to 10^{18} eV (Mücke & Protheroe 2001; Bottacini et al. 2016). Hadronic models are relatively less explored compared to leptonic due to the above stringent requirements, and the complexity of the processes comparing to leptonic model.

Synchrotron emission by a particle depends on the uniform magnetic field density, emitting particle's energy and the pitch angle. The average emitted power of an electron with velocity $\beta = v/c$ is given by (Rybicki & Lightman 1979),

$$P_S = \frac{4}{3}\sigma_T c \gamma^2 \beta^2 U_B \tag{1}$$

Here, σ_T is Thomson scattering cross-section and $U_B = B^2/8\pi$. If there is a distribution of particles in the form of a power-law $N(\gamma) = N_0\gamma^{-p}$, the total emission will be,

$$P_{total} = \int_{\gamma_{min}}^{\gamma_{max}} N(\gamma) P(\nu, \gamma, \theta) d\gamma \quad \propto \nu^{-\frac{p-1}{2}} \tag{2}$$

where p is the power-law index. The critical frequency of an electron, with energy γ and mass m_e, at which most emission occurs, is $\nu_c = \frac{3\gamma^2 eB}{4\pi m_e}$. According to the position of the synchrotron peak (ν_{sync}),

blazars are sub-divided into three classes (Padovani & Giommi 1995): LSP ($\nu_{sync} < 10^{14}$ Hz), ISP ($10^{14} < \nu_{sync} < 10^{15}$ Hz) and HSP ($\nu_{sync} > 10^{15}$ Hz), i.e., low, intermediate and high synchrotron peaked blazars, respectively.

In IC scattering, if $h\nu << m_e c^2/\gamma$, the Thomson scattering cross-section is considered. The scattered photon energy can be approximated as, $\varepsilon_f \approx \gamma^2 \varepsilon_i$. Whereas, if $h\nu \gtrsim m_e c^2/\gamma$, the Klein-Nishina scattering cross-section is used, then $\varepsilon_f \approx \gamma m_e c^2$. The total power emitted by IC scattering,

$$P_{IC} = \frac{4}{3}\sigma_T c \gamma^2 \beta^2 U_{ph} \tag{3}$$

Here, U_{ph} is the energy density of seed photons.

2. Multi-Wavelength Variability of the Blazar Markarian 421

Mrk 421 is one of the closest ($z = 0.031$) HSP type blazar in which the synchrotron peak of the SED is at X-ray frequencies and the high energy peak is at ∼50 GeV (e.g., Abdo et al. 2011; Banerjee et al. 2019). It was the first extragalactic source to be detected at TeV energies (Punch et al. 1992). We study the minutes to days timescale X-ray variability of Mrk 421 using a quasi-continuous observation by *AstroSat* and also compare the same with simultaneous observations at GeV, optical, and near infrared (NIR) wave bands. We calculate variability amplitude and timescale at all wavelengths to check if those are consistent with the leptonic scenario of blazar.

2.1. Data Set

Mrk 421 was observed at X-rays by *AstroSat* on April 23-28, 2019. *AstroSat* is India's first multi-wavelength space telescope launched in 2015. Two instruments on board *AstroSat*, namely, the Soft X-ray Telescope (SXT) and Large Area X-ray Proportional Counter (LAXPC) observe the sky at soft and hard X-ray band (Singh et al. 2016; Yadav et al. 2016). We take SXT data in the energy range $0.7-8$ keV and LAXPC data at $4-20$ keV energy from the *AstroSat* data archive at the Indian Space Science Data Center (ISSDC) [1] and extract the corresponding light curves. Blazar variability at X-ray and other wave bands, including that of Mrk 421, at longer timescales have been studied extensively but that at sub-day timescales has been less common because even the brighter blazars are not detected with high signal to noise at short exposures. We use this data set to probe the sub-day timescale X-ray variability of Mrk 421.

At the GeV energies, we use data from the Large Area Telescope on board *Fermi Gamma-Ray Space Telescope* (*Fermi*-LAT). We use the light curve at 0.1-300 GeV obtained from the Fermi

[1] https://astrobrowse.issdc.gov.in/astro_archive/archive/Home.jsp

Science Support Center (FSSC). The optical flux and polarimetric data were obtained using the St. Petersburg University 40 cm LX-200 telescope and the Crimean observatory 70 cm AZT-8 telescope. Near-infrared observations of Mrk 421 in H-band, simultaneous with the AstroSat observations, were carried out with PRL's 1.2 m telescope at *Mount Abu Infrared Observatory (MIRO)*, India. The multi-wavelength light curves of Mrk 421 during April 16 - May 06, 2019 are shown in Figure 2.

2.2. Results

The variability timescale at all wavelengths are calculated during both increase and decrease of flux using the following equation (Saito et al. 2013; Roy et al. 2019):

$$\tau_d = \Delta t \frac{ln2}{ln(f_2/f_1)}, \tag{4}$$

where f_1 and f_2 are the flux values at time t_1 and t_2, and Δt is the difference between them. The shortest timescale of variability that we find at each band along with the corresponding value of Δt are given in Table 1. Value of τ_d during increase of flux for H-band could not be obtained because the length and sampling of the light curve are not enough for that calculation. In addition, Table 1 exhibits the normalized excess variance at all the above wave bands. In the GeV band, the variance is dominated by the uncertainties in the data. Therefore, the excess variance is negligible and is not shown on the table. The value of τ_d is the shortest at the hard X-ray band, slightly higher at the soft X-ray band and much longer at the optical, NIR as well as GeV bands. This is consistent with the assumption that the X-rays are produced by the highest energy tail of the electron distribution via synchrotron process. A consequence of that assumption is that the variability at the GeV band, being produced by lower energy electrons via IC processes, will be less pronounced, which is also evident.

Table 1: Variability Timescale and Excess Variance at Different Wave Bands

Wave Band	τ_d (increase) (ks)	Δt (ks)	τ_d (decrease) (ks)	Δt (ks)	Normalized Excess Variance
GeV	37.2±23.3	86.4	279.1±256.6	432.0	—
Hard X-Ray	1.5±0.2	2.0	1.1±0.2	1.0	0.29
Soft X-Ray	2.3±1.4	0.6	1.5±1.1	0.6	0.12
R-Band	195.3±89.0	6.2	99.4±7.3	7.3	0.07
H-Band	—	—	366.3±34.5	91.6	0.07

We have found the minimum variability timescale to be 1.1 ks at hard X-ray. Assuming the variability is dominated by radiation cooling due to synchrotron process,

$$t_{cool} \simeq 7.7 \times 10^8 (1+z) \delta^{-1} B^{-2} \gamma_{\rm eff}^{-1} s, \tag{5}$$

where z, δ, B, and $\gamma_{\rm eff}$ are the redshift of the source, Doppler factor of the jet, magnetic field in the emission region, and effective Lorentz factor of the emitting electrons, respectively (Rybicki &

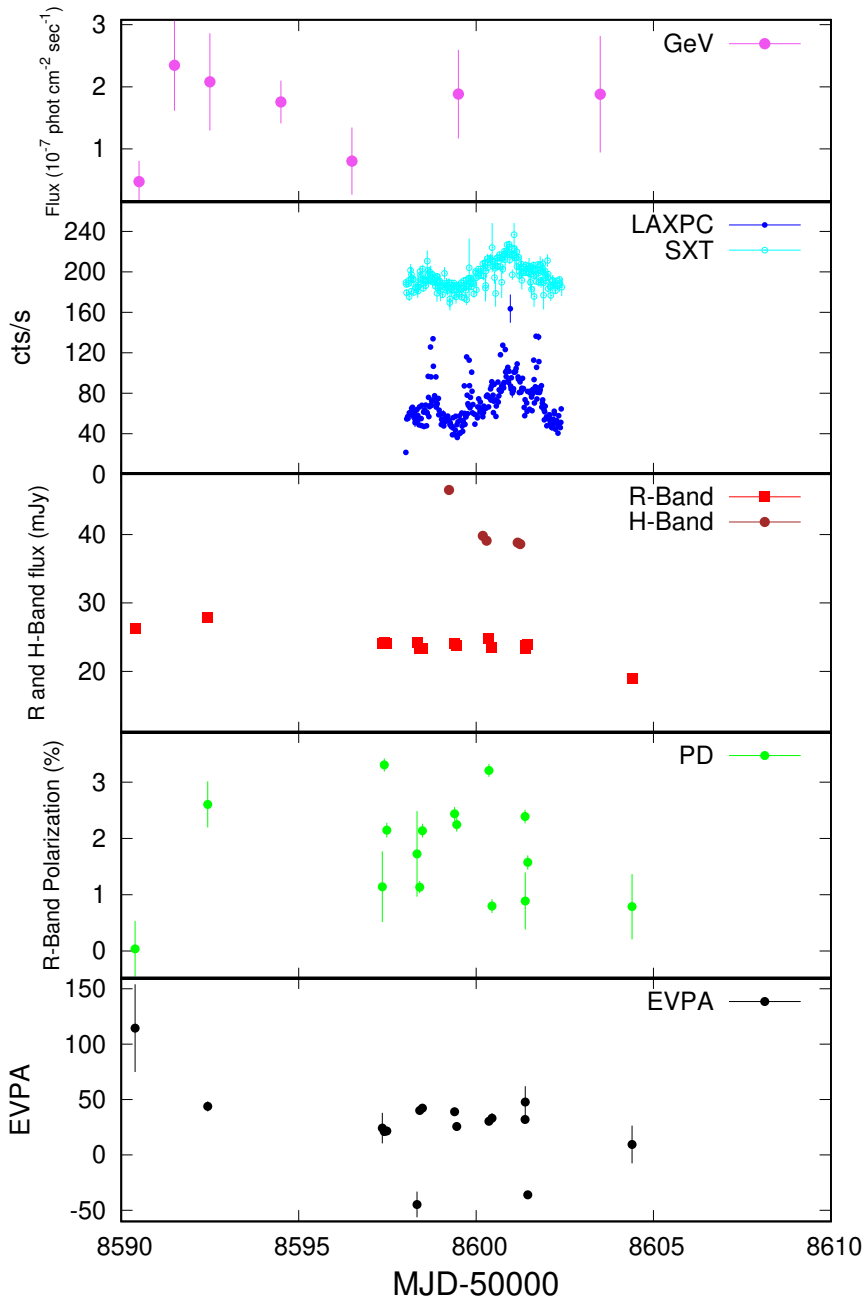

Fig. 2.— From top to bottom, panels display variation of the 0.1−300 GeV γ-ray flux from *Fermi*-LAT in daily bins, hard (4−20 keV) and soft (0.7−8 keV) X-ray flux from *AstroSat*'s LAXPC and SXT, $H-$band flux density from *Mount Abu Infrared observatory* NICS instrument, and $R-$band flux density and optical polarization properties from the St. Petersburg University 40 cm LX-200 telescope and the Crimean observatory 70 cm AZT-8 telescope of Mrk 421 from 2019 April 16 - May 06. The SXT data have been scaled and shifted for clarity.

Lightman 1979). The characteristic frequency of the electron distribution responsible for the emission at the synchrotron peak of the SED is given by (Rybicki & Lightman 1979),

$$\nu_{crit} = 4.2 \times 10^6 \frac{\delta}{1+z} \gamma_{\rm eff}^2 B \; Hz \tag{6}$$

Using z= 0.031, $\delta = 20$, and $\nu_{crit} = 10^{18}$ Hz in the equations 5 and 6, we find $B = 0.5$ Gauss and $\gamma_{\rm eff} = 1.6 \times 10^5$. Alternatively, the energy of the electrons responsible for the GeV emission may be obtained using the inverse-Compton cooling timescale given by (Chiaberge & Ghisellini 1999),

$$t_{cool}^{IC} \simeq 3.0 \times 10^7 U_{rad}^{-1} \gamma_{\rm eff}^{-1} s, \tag{7}$$

where U_{rad} is the radiation energy density. Using $t_{cool}^{IC} = 100$ ks and $U_{rad} = 10^{-2}$ erg cm^{-3} we obtain $\gamma_{\rm eff} = 3 \times 10^4$. Here, we estimate U_{rad} to be approximately equal to the magnetic energy density.

2.3. Discussion

From Table 1, it can be seen that in the above observations, the variability timescale is shortest at the hard X-ray band and increasingly longer at soft X-ray, optical and NIR bands as well as in the GeV band. This is consistent with the model in which the X-ray to optical-NIR emission in Mrk 421 are generated by synchrotron radiation by the relativistic electrons in the jet. The slower variability timescale of GeV emission is also expected when the GeV emission may produce via SSC process by electrons having energy lower than those producing the X-rays. The amplitude of variability, as indicated by the normalized excess variance, is also larger at the X-ray energies than the lower energy wave bands. It can be seen from Table 1 that τ_d during increase and decrease at all wavebands are not systematically different. In blazar variability it is usually assumed that the timescale of acceleration of electrons to the highest energies (e.g., $\gamma_{\rm eff} = 10^5$ in this case) is faster than the cooling timescale such that the acceleration may be considered instantaneous. However, that will indicate τ_d during increase will be systematically shorter than that during decrease, which is not the case here. This implies that the acceleration timescale may not be negligible compared to the cooling timescales and may be constrained using short-timescale variability as analyzed here. The obtained value of the magnetic field, maximum energy of electrons are also consistent with those obtained from studies involving fitting the SED with physical models (Abdo et al. 2010; Banerjee et al. 2019). The above quantitative results, obtained from the shortest end of the large range of timescales at which blazars vary, are consistent with the standard leptonic scenario, in which the lower energy peak at X-ray of the SED of Mrk 421 is due to synchrotron radiation by the relativistic electrons in the jet.

3. Correlated Hard-Soft X-ray Variability of the Blazars Mrk 421 and 1ES 1959+650

The higher-amplitude variability of blazars at weeks to months timescale is believed to be caused by the crossing of shock waves through the emission region which energizes the quiescent particles (e.g., Marscher 2016; Böttcher 2019). There is significant variability, factor of a few to even an order of magnitude, at minutes to days timescales, particularly at the X-ray and γ-ray energies. Sub-day timescale variability of blazars may be caused by the acceleration and radiative cooling of the emitting particles (Zhang 2002; Ravasio et al. 2004) as well as turbulence in the magnetic field. Based on the physical mechanisms, the emission at different bands may be correlated or not.

Here, we analyse *AstroSat*'s SXT & LAXPC data of two HSP blazars Mrk 421 and 1ES 1959+650 at multiple epochs during 2016-19. We study cross-correlation between simultaneous soft X-ray and hard X-ray light curves along with precise estimates of the time lag and its uncertainties. We discuss the results and their implications regarding the emission mechanism and physical properties of the jet.

3.1. AstroSat Data

We analyze soft X-ray light curves at the energy range ($0.7-7$ keV) from the SXT instrument and hard X-ray light curves ($7-20$ keV) from the LAXPC instrument onboard *AstroSat* for three epochs of 1ES 1959+650 and five epochs of Mrk 421 during 2016-19. We use a lower limit of 0.7 keV for our SXT light curves to avoid certain instrumental features (e.g., Shah et al. 2021) that are present at energies lower than that. We set the upper limit of LAXPC to 20 keV because the background noise starts to dominate above that energy (e.g., Hota et al. 2021). The simultaneous light curves of SXT and LAXPC for multiple epochs of 1ES 1959+650 and Mrk 421 are shown in Figures 3, 4.

3.2. Cross-Correlation Analysis

We cross-correlate the hard and soft X-ray light curves of both blazars for each of the epochs using the discrete cross-correlation function (Edelson & Krolik 1988) method. The cross-correlation function between the hard and soft X-ray variability may indicate whether the fluctuations at those two bands are causally related. In order to test the significance of the cross-correlation results we simulate 100 each of hard and soft X-ray light curves from their power-spectral density (PSD) using the algorithm by Timmer & Koenig (1995) by considering the power-spectral shape and slope from Chatterjee et al. (2018) for both sources. Then we cross-correlate between the simulated light curves and calculate significance level at 99% and 95% (see Figure 5). We calculate time delay and its uncertainty between those two bands using a model-independent Monte-Carlo method, namely, flux

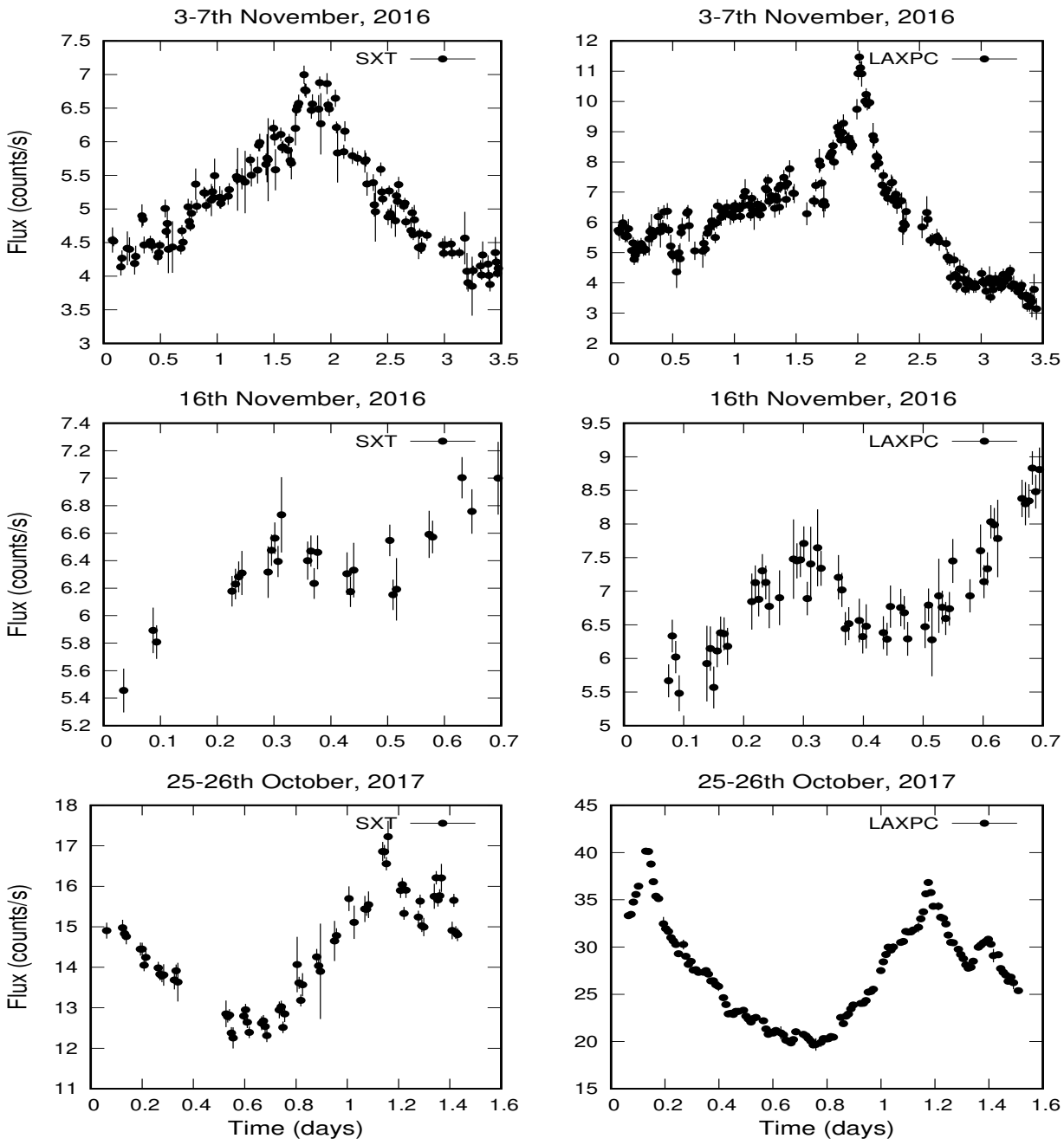

Fig. 3.— Black solid circles denote X-ray count rates of the blazar 1ES 1959+650 at multiple epochs during 2016-2017 observed by the Indian space telescope *AstroSat*. The left and right panels show the X-ray light curves at $0.7-7$ keV from SXT and that at $7-20$ keV from LAXPC instrument, respectively, onboard *AstroSat*.

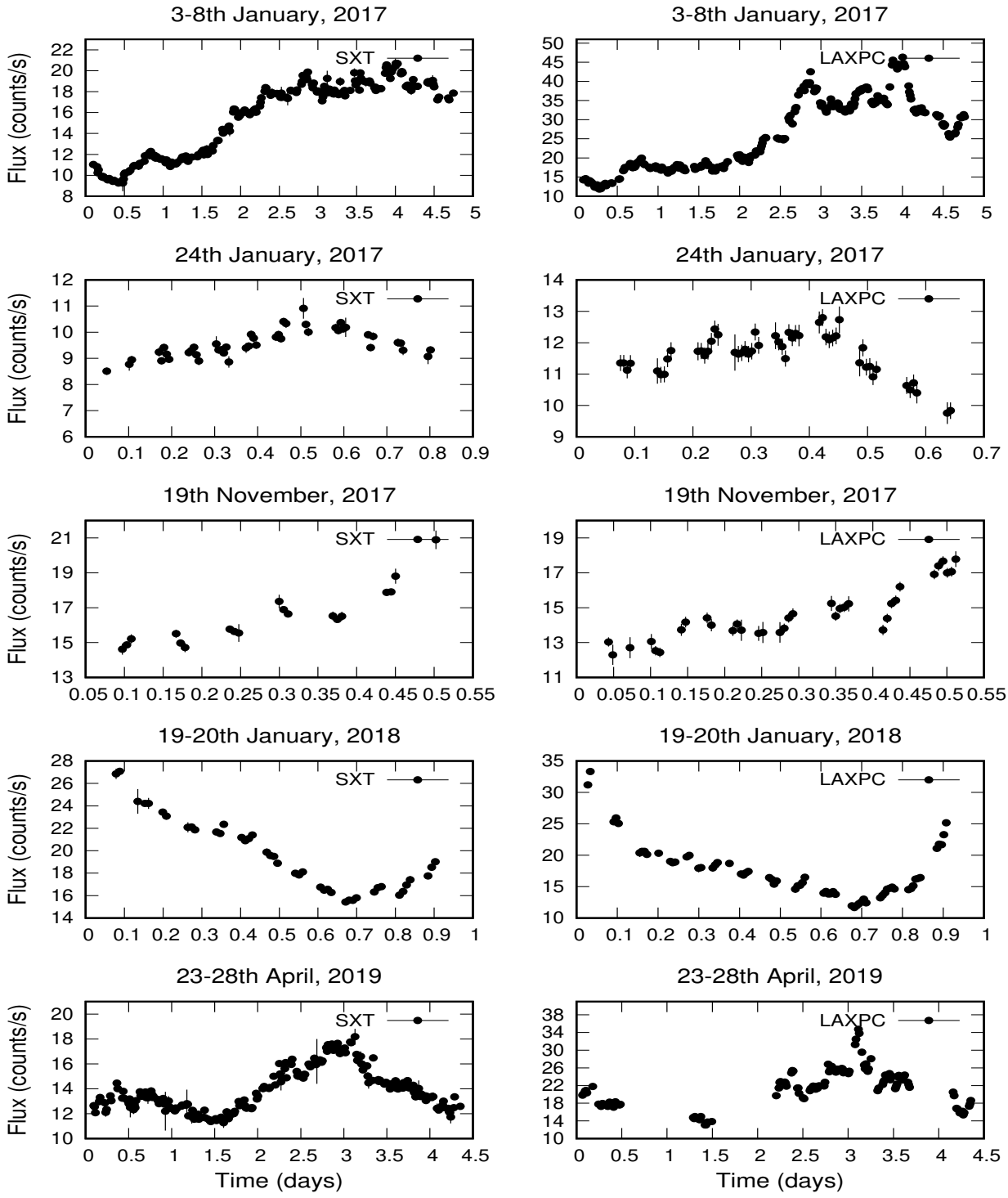

Fig. 4.— Black solid circles denote X-ray count rates of the blazar Mrk 421 at multiple epochs during 2016-2019 observed by the Indian space telescope *AstroSat*. The left and right panels show the X-ray light curves at $0.7-7$ keV from SXT and that at $7-20$ keV from LAXPC instrument, respectively, onboard *AstroSat*.

randomization and random subset selection or FR-RSS (Peterson et al. 1998; Sun et al. 2018).

We find that the hard and soft X-ray variability are strongly correlated with at least 95% confidence level in all cases. The cross-correlation functions are symmetric/asymmetric in shape around its maximum. Therefore, we have reported both peak and centroid lag in Table 2. In a few cases, e.g., in the epochs 2016 November 16 of 1ES 1959+650 and 2018 January 19-20 of Mrk 421, the time lags (centroid) are consistent with zero within their uncertainties. Some other light curves exhibit a significant lag of $\sim$hour, i.e., variability at the hard band lagging those at the soft X-rays or *vice versa*, termed as hard lag and soft lag, respectively. In the convention we use, a positive value of the time delay indicates hard lag and a negative time delay denotes a soft lag. For example, 1ES 1959+650 in the 2017 epoch and Mrk 421 in the 2017 January 3-8 epoch exhibit significant hard lag (centroid) while Mrk 421 shows a significant soft lag (centroid) during the 2017 January 24 epoch, beyond the corresponding uncertainty values.

Table 2: Time Lag and its uncertainty of the correlated soft ($0.7-7$ keV) and hard ($7-20$ keV) X-ray variability of the blazars 1ES 1959+650 (upper) and Mrk 421 (lower) at different epochs during $2016-19$. Positive values of time delay denote a hard lag, i.e., the hard band variability lags those at the soft band. The uncertainties have been computed using the FR-RSS technique.

Observation Date	Peak lag (hr)	Centroid lag (hr)
2016 November 3-7	$1.63^{+0.3}_{-0.21}$	$0.99^{+0.48}_{-0.41}$
2016 November 16	$-0.02^{+0.66}_{-0.42}$	$0.09^{+0.53}_{-0.45}$
2017 October 25-26	$1.17^{+0.8}_{-0.18}$	$1.98^{+0.36}_{-0.33}$
Observation Date	**Peak lag (hr)**	**Centroid lag (hr)**
2017 January 3-8	$-0.05^{+0.45}_{-0.15}$	$7.35^{+0.95}_{-0.76}$
2017 January 24	$-4.39^{+0.6}_{-0.93}$	$-4.46^{+0.58}_{-0.52}$
2017 November 19	$0.71^{+0.57}_{-0.51}$	$0.65^{+0.30}_{-0.28}$
2018 January 19-20	$-0.9^{+0.48}_{-0.54}$	$-2.07^{+2.20}_{-0.38}$
2019 April 23-28	$2.14^{+1.44}_{-1.53}$	$2.86^{+0.58}_{-0.44}$

3.3. Discussion

Here we use the SXT and LAXPC energy ranges, i.e., $0.7-7$ keV and $7-20$ keV, respectively which include the lower energy peak of the SED of the two HSP blazars as well as its decaying part beyond the peak energy (Abdo et al. 2011; Kapanadze et al. 2018; Giommi et al. 2021). Therefore, the electrons responsible for generating the X-rays are at the peak of their energy distribution. The cooling timescales of such high energy electrons are short ($\sim$hr). Therefore, it is assumed that they are physically located in a compact region and undergo acceleration and cooling at approximately the

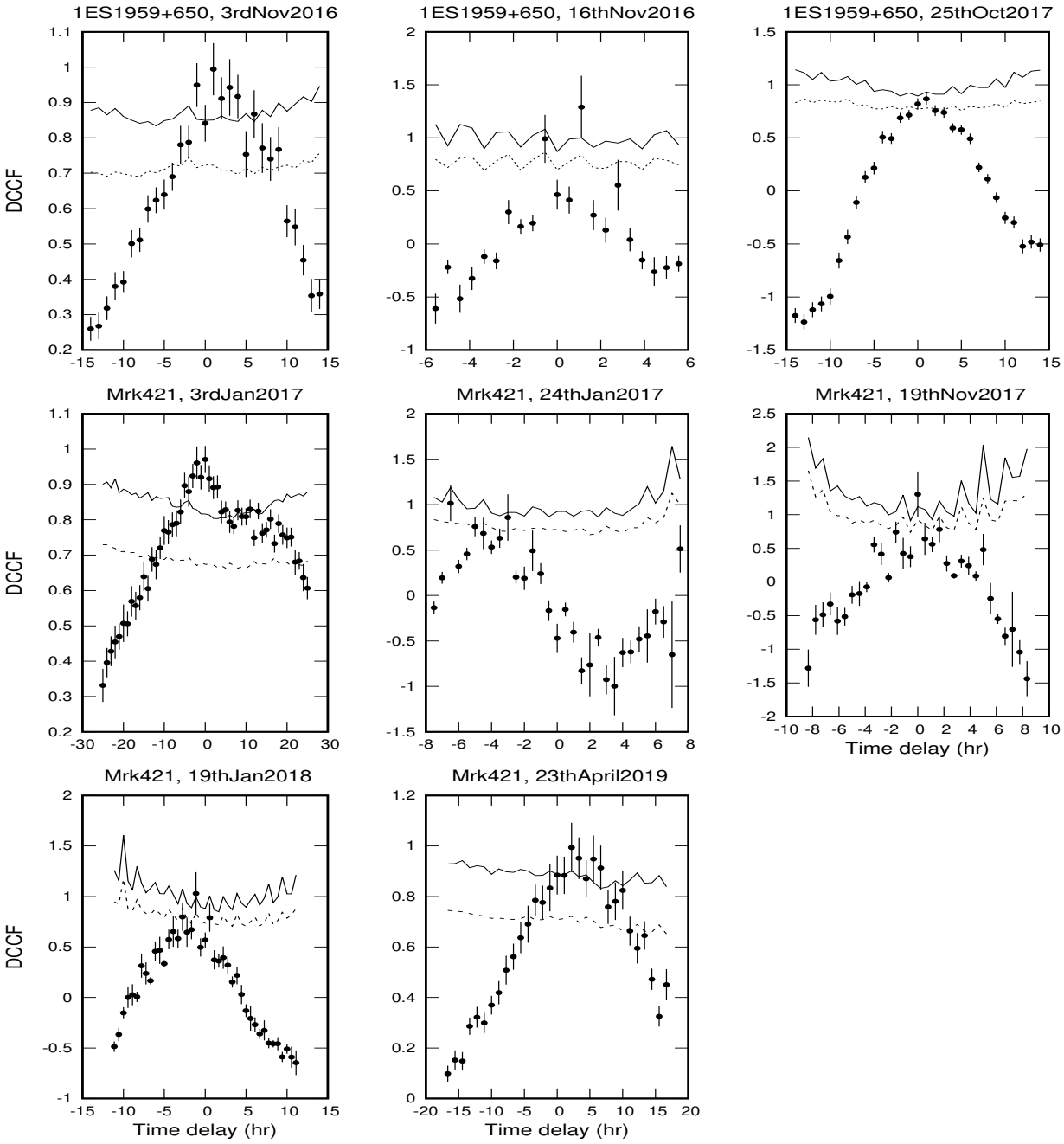

Fig. 5.— Black solid circles denote the discrete cross-correlation functions of the soft ($0.7-7$ keV) and hard ($7-20$ keV) X-ray variability of the blazars 1ES 1959+650 and Mrk 421 during the epochs shown in Figures 3 and 4. The dashed and solid lines indicate 95% and 99% significance levels, respectively. Positive values of time delay denote a hard lag, i.e., the hard band variability lags those at the soft band.

same time. That is consistent with the strong correlation with zero or very short time delay between the hard and soft X-ray variability as we have found here.

In blazar jets the particles are accelerated by moving shocks through, e.g., a first order Fermi acceleration mechanism (Blandford & Eichler 1987; Kirk et al. 1998; Kusunose et al. 2000; Zhang et al. 2002). The acceleration timescale (t_{acc}) is proportional to the final energy achieved by the particles while synchrotron cooling timescale (t_{cool}) is inversely proportional to the energy of the particle. The particles will reach the highest energy when $t_{acc} \simeq t_{cool}$, whereas below the highest energy $t_{acc} << t_{cool}$ (Böttcher 2019), i.e., the cooling timescale dominates. For HSP blazars, the electrons that emit X-rays are at the peak of their energy distribution and we may assume $t_{acc} \simeq t_{cool}$ (Zhang 2002). That is consistent with the observed result that we see zero time lag in some cases between the hard and soft X-ray variability while in some cases we do find a small amount ($\sim$ hrs) of soft or hard lag. In particular, hard lag indicates the acceleration timescale is longer than our time resolution and we are able to probe it through our light curves and inter-band time delays.

The soft/hard lag may be expressed as below:

$$\tau_{soft} = t_{cool}(E_{soft}) - t_{cool}(E_{hard}) \tag{8}$$

$$\tau_{hard} = t_{acc}(E_{hard}) - t_{acc}(E_{soft}) \tag{9}$$

The energy dependent acceleration and cooling timescales may be given as the following (Zhang et al. 2002; Ravasio et al. 2004):

$$t_{acc}(E) = 9.65 \times 10^{-2}(1+z)^{3/2}\xi B^{-3/2}\delta^{-3/2}E^{1/2} \ \text{s} \tag{10}$$

$$t_{cool}(E) = 3.04 \times 10^{3}(1+z)^{1/2}B^{-3/2}\delta^{-1/2}E^{-1/2} \ \text{s} \tag{11}$$

Here, E, z, B and δ are the energy of the emitted photon, redshift of the blazar, magnetic field at the emission region and the Doppler factor, respectively. ξ is the so-called 'acceleration parameter' or 'acceleration efficiency'.

Substituting Equations (10) and (11) into Equations (8) and (9), one gets (as in Kazanas et al. 1998; Zhang et al. 2006):

$$B\delta^{1/3} = 209.91 \times \left(\frac{1+z}{E_s}\right)^{1/3} \left[\frac{1-(E_s/E_h)^{1/2}}{\tau_{soft}}\right]^{2/3} \ \text{G} \tag{12}$$

$$B\delta\xi^{-2/3} = 0.21 \times (1+z){E_h}^{1/3} \left[\frac{1-(E_s/E_h)^{1/2}}{\tau_{hard}}\right]^{2/3} \ \text{G} \tag{13}$$

Here, E_s and E_h are the logarithmic mean energy of the corresponding soft and hard energy bands,

respectively. In the case of Mrk 421, considering the soft lag (centroid lag) and the hard lag, we obtain the value of B to be in the range $0.05-0.12$ G and the acceleration parameter is $\xi \sim 10^4$ by assuming $\delta \sim 10-20$. In the case of 1ES 1959+650, there is a hard lag in 2017. Using this time lag, we obtain $B\delta\xi^{-2/3} = 1.0\times10^{-3}$. If $B \sim 0.1$ G and $\delta = 10$, the value of ξ is $\sim 10^4$. The acceleration parameter ξ is the ratio of the mean free path to the gyroradius (λ/r_g) in the acceleration region (Inoue & Takahara 1996; Baring et al. 1997, 2017). A large value of the acceleration parameter implies that the mean free path of scattering is large compared to the gyroradius (r_g). For relativistic electrons $r_g = \frac{\gamma mc^2}{eB}$. Assuming $B = 0.1$ G, $r_g \sim 10^4\gamma$ cm. That implies the mean free path of the electrons with $\gamma \sim 10^2$ will be 10^{10} cm for $\xi = 10^4$. If we assume the electrons are moving at a speed close to that of light, they will traverse $\sim 10^5\lambda$ in an interval equal to the acceleration timescale $\sim 10^5$ s. Therefore, they will undergo $\sim 10^5$ scatterings in the acceleration region to be accelerated to the maximum energy ($\gamma \sim 10^5$) starting from $\gamma \sim 10^2$. That indicates the energy amplification in each scattering, assuming it is uniform at all values of initial energy, is $7\times10^{-3}\%$. If we make the same assumptions as above the electrons will undergo 10^3 scatterings in order to reach $\gamma = 10^5$ from $\gamma = 10^4$. In that case, the energy amplification is 0.23% in each scattering.

4. Sub-Day Timescale X-ray Spectral Variability

In blazars, not only the total flux fluctuates over time but the spectral properties, e.g., the frequency of the peak and shape of spectrum also vary. Here, we focus on the X-ray spectral variation of two HSP blazars, namely, Mrk 421 and 1ES 1959+650, at minutes to days timescales. The lower energy peak of their SED is at the X-ray energy range (Abdo et al. 2011; Banerjee et al. 2019; Böttcher & Dermer 2010). Therefore, study of X-ray emission provides information about the emissions behavior by the highest energy electrons in the jet.

These two blazars have been observed with AstroSat at several epochs during 2016-19 giving rise to X-ray light curves and spectra at minutes to days timescales (Hota et al. 2021; Chandra et al. 2021; Markowitz et al. 2022). Here, we aim to find the best-fit model of the X-ray spectra during those epochs. We also study the time resolved spectra to see variability at sub-day timescales and find correlation between their best-fit spectral parameters. We explore the physical explanation of correlation trends and compare the results with that of a theoretical model considering a multi-zone emission region in order to constrain the geometric and emission parameters in the jets of those blazars.

4.1. X-ray Data

The X-ray data of the blazars Mrk 421 and 1ES 1959+650 used in this work are from *AstroSat* and the *Neil Gehrels Swift Observatory*. We use data from *AstroSat*'s SXT and LAXPC instruments of Mrk 421 and 1ES 1959+650 of the same epochs mentioned in the previous section during 2016-19 (Das & Chatterjee 2023). We also collect archival data of *Swift*-XRT analysed *Swift*-XRT online building tool (Evans et al. 2009), the duration of which overlaps with *AstroSat* observations of these sources.

Table 3: Best-fit parameter values from log-parabola modeling of XRT+SXT+LAXPC spectra.

Source	Epoch	Constant*	α	β	E_{peak} (keV)	$\log_{10}$Flux in CGS ($0.7-20$ keV)	χ^2/dof
1ES 1959+650	2016, 3-7th Nov	0.77 ± 0.02	1.99 ± 0.01	0.35 ± 0.02	0.98 ± 0.05	-9.42 ± 0.15	1.07
	2016, 16th Nov	0.81 ± 0.03	1.97 ± 0.03	0.42 ± 0.03	1.09 ± 0.09	-9.34 ± 0.006	1.03
	2017, 25-26th Oct	0.77 ± 0.01	1.72 ± 0.01	0.32 ± 0.01	2.69 ± 0.07	-8.92 ± 0.12	1.17
Mrk 421	2017, 3-8th Jan	0.71 ± 0.01	1.81 ± 0.01	0.26 ± 0.02	2.25 ± 0.05	-8.92 ± 0.08	1.4
	2017, 24th Jan	0.71 ± 0.02	1.97 ± 0.02	0.33 ± 0.02	1.07 ± 0.07	-9.12 ± 0.01	1.11
	2017, 19th Nov	0.77 ± 0.02	1.91 ± 0.02	0.37 ± 0.02	1.30 ± 0.08	-9.00 ± 0.003	0.95
	2018, 19-20th Jan	0.75 ± 0.01	2.02 ± 0.01	0.31 ± 0.01	0.91 ± 0.05	-8.89 ± 0.02	1.38
	2019, 23-28th April	0.69 ± 0.01	1.94 ± 0.01	0.12 ± 0.01	1.78 ± 0.12	-8.97 ± 0.04	1.44

* Constant is the flux normalization factor of LAXPC corresponding to SXT.

4.2. Spectral Analysis

We carry out the spectral analysis using XSPEC (version 12.10), a tool of `HEASoft`. We analyse SXT and LAXPC spectra in the energy range $0.7-20$ keV and XRT spectra at $0.7-7$ keV range. The combined spectra are fit using the log-parabola model in XSPEC. There is a flux normalization offset between different instruments, which is represented by a constant factor in the spectral modeling. The Galactic hydrogen column density n_H values for the line of sight containing Mrk 421 and 1ES 1959+650 are fixed at 1.92×10^{20} cm^{-2} and 1.07×10^{21} cm^{-2} (Kalberla et al. 2005), respectively. We add 3% systematic error and do the correction of gain for the SXT spectrum (Chandra et al. 2021). The time-averaged spectra are satisfactorily fit by the log-parabola model and the best-fit parameters of the spectral are listed in Table 3. To study the nature of spectral variability at sub-day timescales, we divide the data of all epochs of the two blazars into time segments of length 10 ks. For each time bin, we fit SXT and LAXPC spectrum of each epoch with the log-parabola model at $0.7-20$ keV. We estimate the unabsorbed flux values at $0.7-20$ keV from fitted time-resolved spectra and determine the energy flux light curves (Figure 6). We get the best-fit values in every time bin of each epoch and the correlation between these spectral parameters are shown in Figures 9 and 10. The correlation strength and their probability of significance are shown in Table 4.

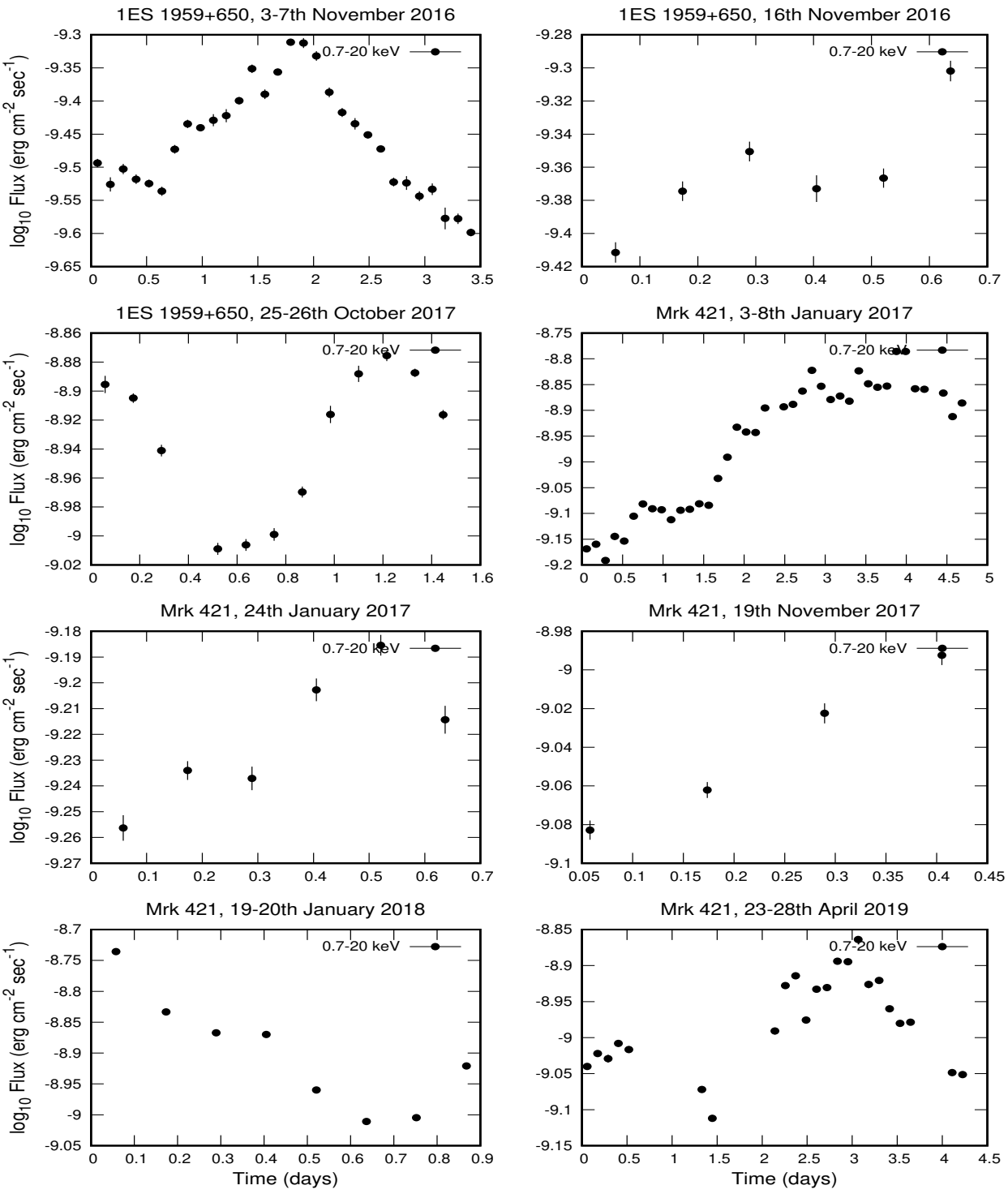
1ES 1959+650, 3-7th November 2016
1ES 1959+650, 16th November 2016
1ES 1959+650, 25-26th October 2017
Mrk 421, 3-8th January 2017
Mrk 421, 24th January 2017
Mrk 421, 19th November 2017
Mrk 421, 19-20th January 2018
Mrk 421, 23-28th April 2019
0.7-20 keV
log10 Flux (erg cm-2 sec-1)
Time (days)

Fig. 6.— The energy flux light curves of the blazars 1ES 1959+650 and Mrk 421 from time-resolved spectroscopy with 10 ks bins obtained from fitting the *AstroSat* data with log-parabola model at multiple epochs during 2016-19.

The spectral parameters α, β and corresponding peak energy (E_{peak}) in the log parabola model are varying significantly within hours and also from one epoch to another. The dependence of parameters on flux values shows that α is decreasing and E_{peak} is increasing with increasing flux for all observations, but there is no clear pattern in the variation of β. On the other hand, α has an inverse relation with E_{peak} while β shows a weak correlation with the same, and α and β have a trend of anti-correlation with each other.

4.3. Theoretical Modeling of Jet Emission

In order to interpret the spectral variability found above we compare it to that obtained from a theoretical model of blazar emission variability. Theoretical model of blazar emission has been carried out by several authors (Graff et al. 2008; Marscher 2014; Chen 2014; Banerjee et al. 2019; Liu et al. 2023). A relatively simplistic assumption of such models is that of considering a spherical emission region where electrons are homogeneously distributed. The electrons are instantaneously energized by, e.g., crossing of a shock wave, and subsequently cool via radiation in the presence of a homogeneous magnetic field. This one-zone model has been successful in explaining the broadband SED of blazars in many cases (Abdo et al. 2010; Kapanadze et al. 2018). On the other hand, blazar variability is stochastic in nature, having short-timescale fluctuations. Sometimes, uncorrelated variability of orphan flares are detected in multi-wavelength observations (Rani et al. 2013; Wierzcholska et al. 2019). Typical one-zone models have not been equally successful in explaining the such detailed time variability properties of blazars. Multi-zone models have been proposed in order to address that. Many authors have explored different geometrical approaches in such modeling (e.g., Graff et al. 2008; Joshi & Böttcher 2011; Marscher 2014). In multi-zone scenarios, the value and orientation of the magnetic field may not be uniform throughout the emission region. The electrons in each zone get energized and radiatively cool independently from the neighboring zones. Such models provide more realistic results of timing and spectral properties of blazars. We have discussed one such multi-zone model below.

In this model, a cylindrical emission region is assumed along the jet axis with a viewing angle θ. The emission region consists of multiple cells of equal size, having individual electron distribution and magnetic field (Barat et al. 2022; Kundu et al. 2022). In each cell, the initial distribution of electron energy is a power law given by $N(\gamma) = N_0\,\gamma^{-s}$, where γ is the Lorentz factor of electrons with lower and upper limits γ_{min} and γ_{max}, respectively while s and N_0 are constants. The electron energy evolves as $d\gamma/dt = -k_2\gamma^2$ due to radiative cooling. Here $k_2 = \frac{4\sigma_T}{3m_ec}(U_B + U_R)$, σ_T is the Thomson scattering cross-section, U_B is the magnetic energy density and U_R is the radiation energy density. To simulate X-ray emission by the synchrotron process as is the case for the two HSP blazars discussed here, we use a set of input parameters for our model, which are listed in Table 5.

We simulate light curves at soft X-ray ($0.7-7$ keV) and hard X-ray ($7-20$ keV) light curves

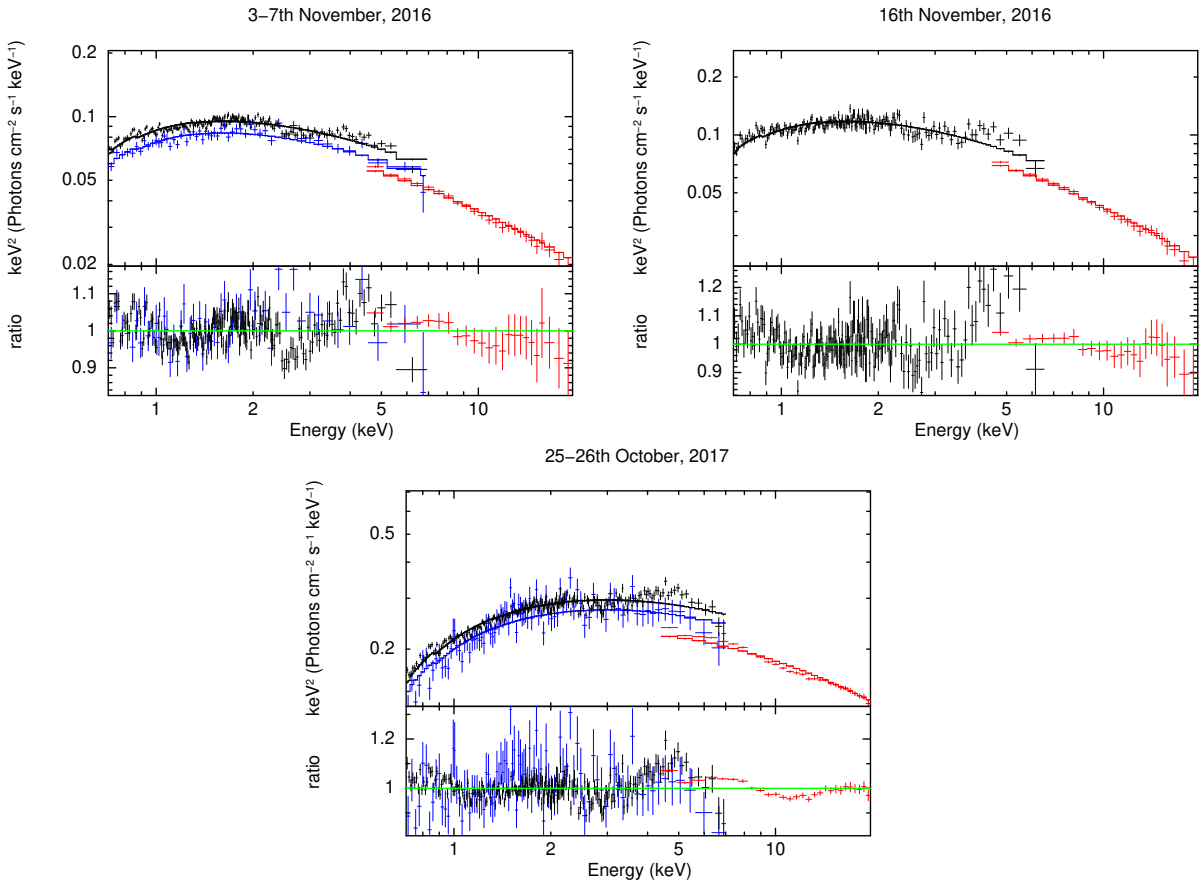

Fig. 7.— XRT (blue), SXT (black) and LAXPC (red) data points and the best-fit log-parabola model of the combined spectra (solid lines) of the blazar 1ES 1959+650 during three epochs in 2016-17.

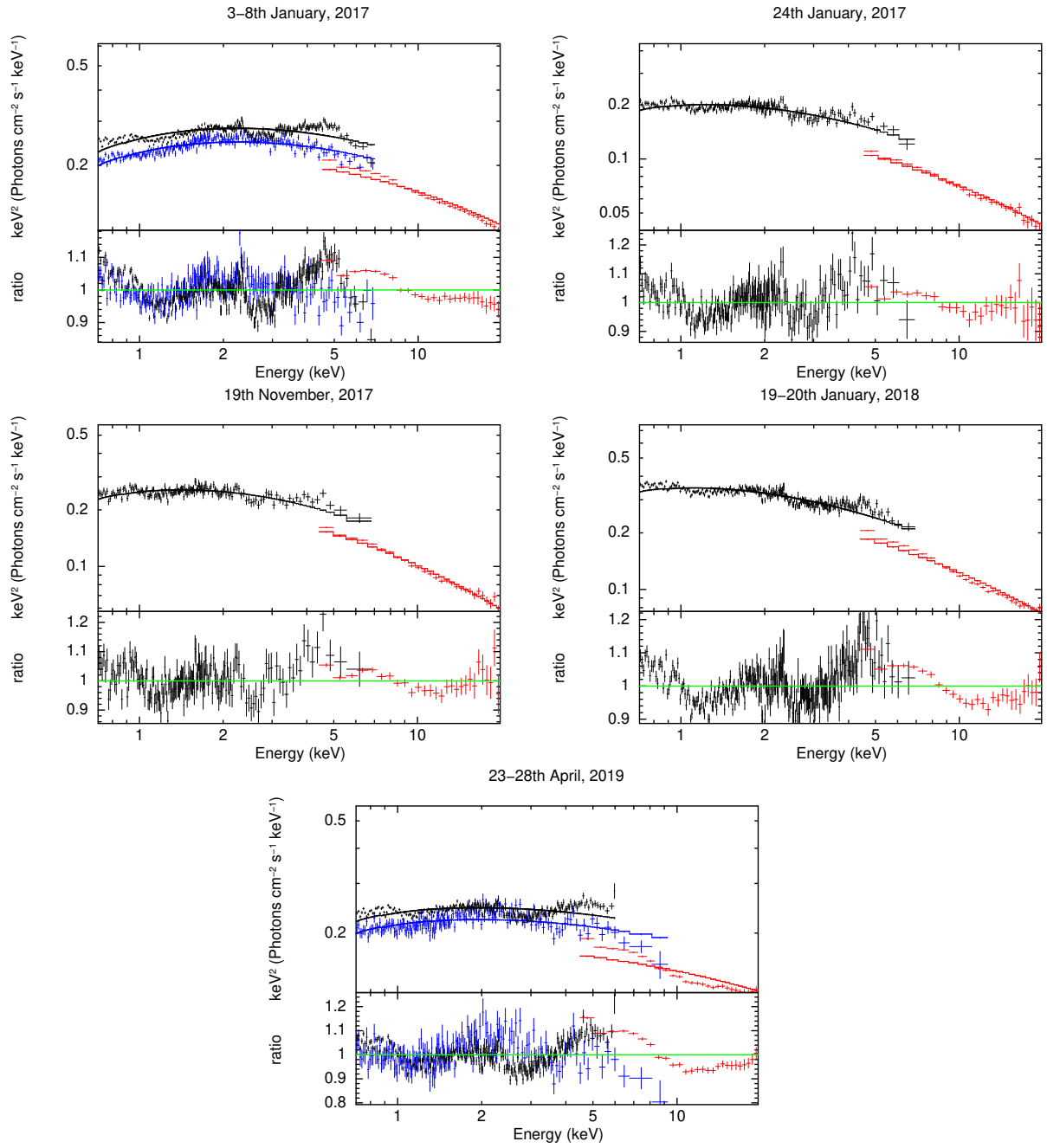

Fig. 8.— XRT (blue), SXT (black) and LAXPC (red) data points and the best-fit log-parabola model of the combined spectra (solid lines) of the blazar Mrk 421 during five epochs in 2017-19.

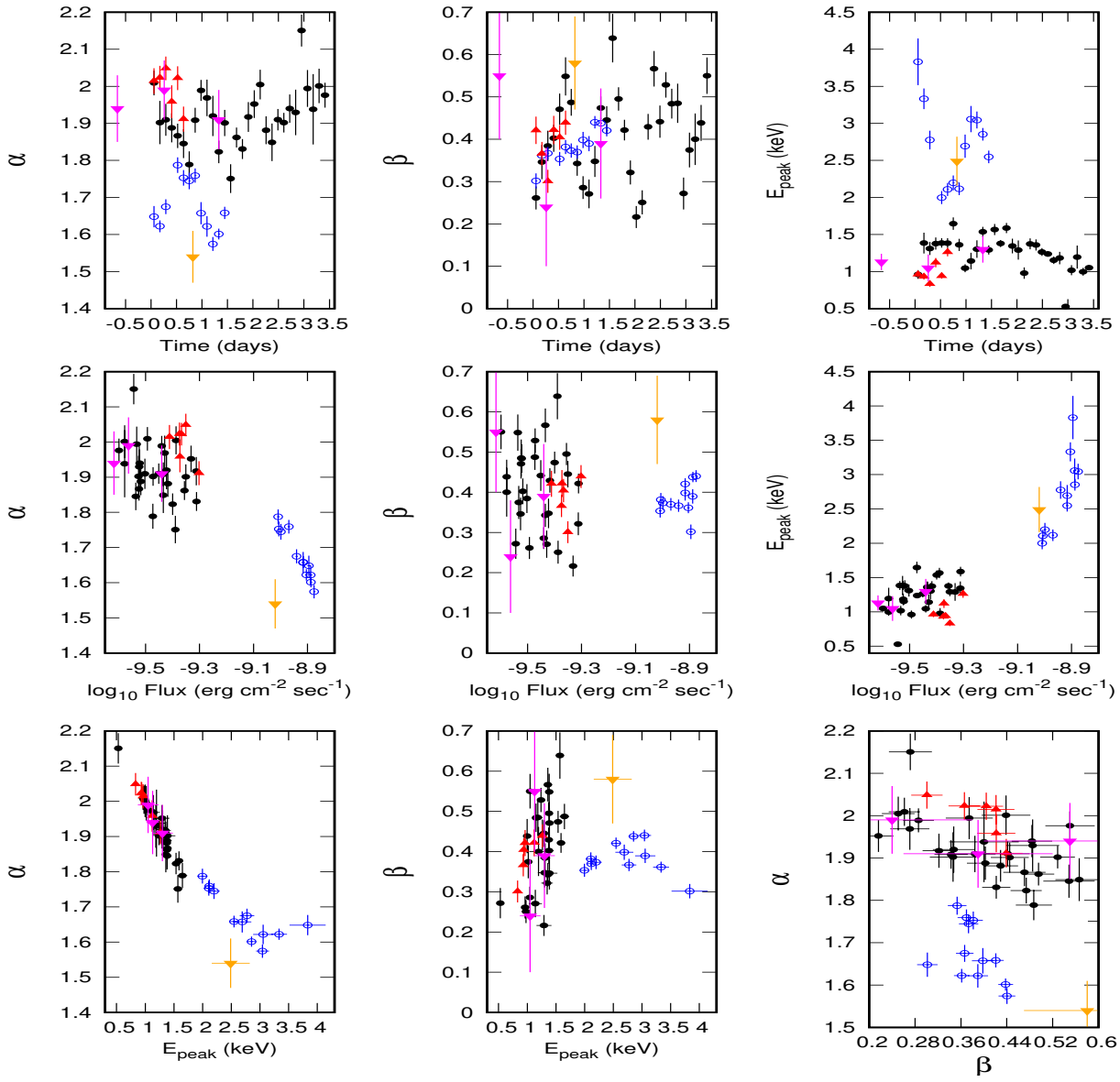

Fig. 9.— Correlation between best-fit spectral parameters of the log-parabola model from time-resolved spectroscopy at 10 ks binning of the *AstroSat* data of the blazar 1ES 1959+650. Black solid circles, red triangles and blue open circles denote the 2016 Nov 3, 2016 Nov 16, and 2017 Oct 25 epochs, respectively. The inverted triangles (orange and magenta for 2016 Nov 3 and 2017 Oct 25 epoch respectively) denote *Swift*-XRT observations.

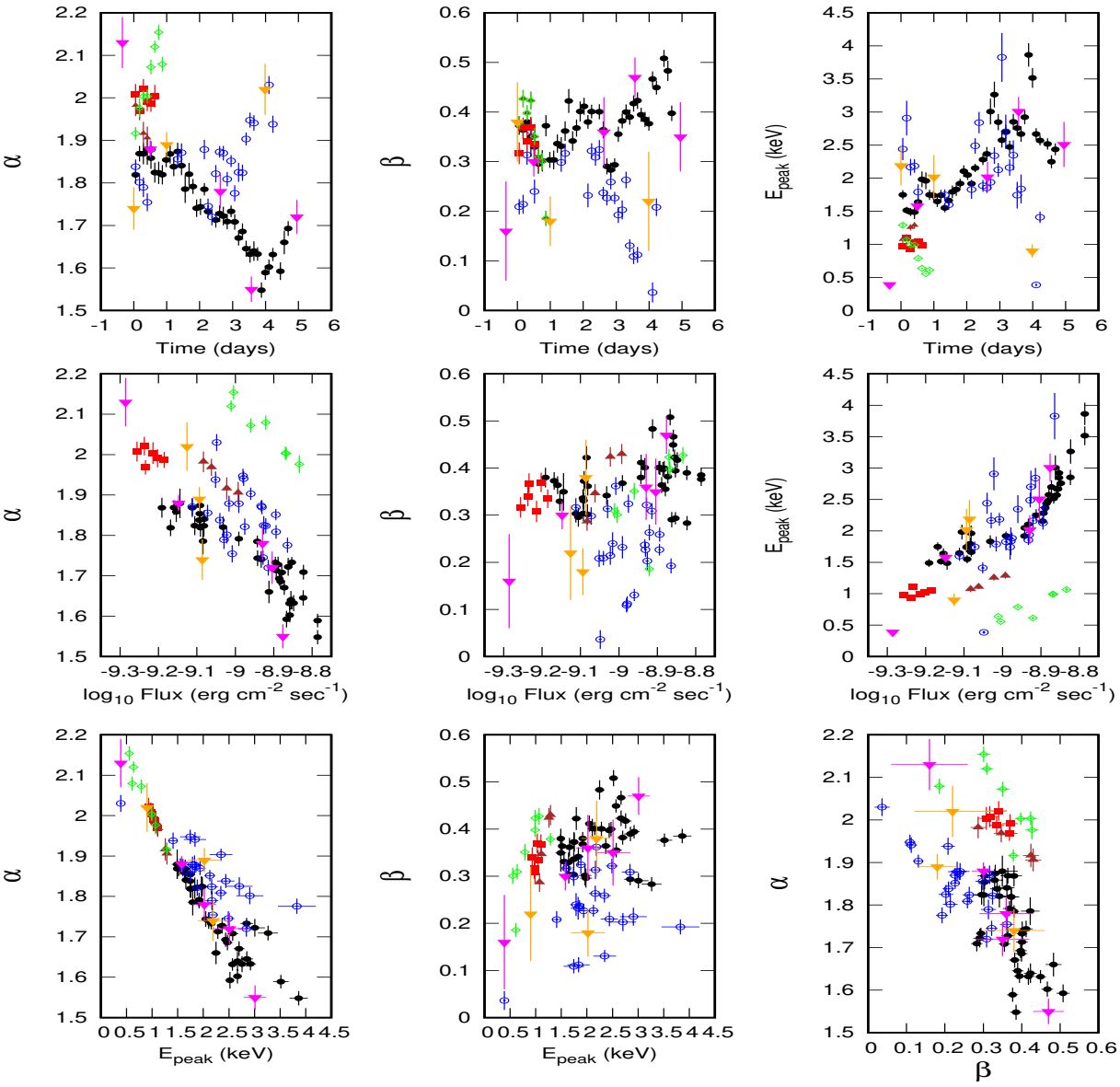

Fig. 10.— Correlation between best-fit spectral parameters of the log-parabola model from time-resolved spectroscopy at 10 ks binning of the *AstroSat* data of the blazar Mrk 421. Black solid circles, red filled squares, maroon triangles, green diamonds, and blue open circles denote the 2017 Jan 3, 2017 Jan 24, 2017 Nov 19, 2018 Jan 19, and 2019 Apr 23 epochs, respectively. The inverted triangles (orange and magenta for 2017 Jan 3 and 2019 Apr 23 epoch respectively) denote *Swift*-XRT observations.

Table 4: Spearman's rank correlation coefficients between the best-fit parameters from fitting the observed spectra of Mrk 421 and 1ES 1959+650 with the log-parabola model.

Mrk 421	3-8th Jan, 2017		23-28th April, 2019	
	r	p	r	p
$\alpha - F_{(0.7-20keV)}$	-0.9	3e-15	-0.41	0.05
$\alpha - E_{peak}$	-0.9	4e-15	-0.41	0.05
$\beta - F_{(0.7-20keV)}$	0.34	0.03	-0.016	0.94
$\beta - E_{peak}$	-0.27	0.09	0.1	0.62
$E_{peak} - F_{(0.7-20keV)}$	0.95	1e-21	0.58	0.003
$\alpha - \beta$	-0.6	3e-5	-0.63	0.001
1ES 1959+650	3-7th Nov, 2016		25-26th Oct, 2017	
	r	p	r	p
$\alpha - F_{(0.7-20keV)}$	-0.34	0.06	-0.97	1e-7
$\alpha - E_{peak}$	-0.94	5e-15	-0.84	6e-4
$\beta - F_{(0.7-20keV)}$	-0.15	0.4	0.47	0.12
$\beta - E_{peak}$	0.44	0.015	0.006	0.98
$E_{peak} - F_{(0.7-20keV)}$	0.34	0.06	0.84	5e-4
$\alpha - \beta$	-0.64	1e-4	-0.51	0.09

* r is Spearman's correlation coefficient, p is null hypothesis probability.

** Two epochs, with total exposure times of several days, for each of the blazars have been used.

Table 5: Fixed parameter values used in the theoretical modelling of jet emission.

Model Parameter	Value
Bulk Lorentz factor (Γ)	15
Doppler factor (δ)	20
Viewing angle with jet axis (θ) in degree	2.7
Slope of electron distribution (s)	2.1
Minimum Lorentz factor of electron (γ_{min})	100
Magnetic field in the first cell (B_i) in G	0.2
Magnetic field in the last cell (B_f) in G	0.1

of duration ~ 5 days and compute the spectral variation of the X-ray emission within $0.7-20$ keV energy range at intervals of 5 ks for two different cases. In one case, radiative cooling dominates the process. We fix γ_{max} at a high value ($10^5 - 10^6$) in each cell such that the synchrotron peak is at keV energies as observed in the blazars in our sample. In another case, we consider gradual acceleration by increasing the value of γ_{max} in successive cells downstream. For these two cases, we fit the $0.7-20$ keV spectra with a log-parabola function at each interval. We get the correlation of best-fit spectral parameters of the above two cases, in the same method applied to the observed data (Figures 11, 12).

4.4. Discussion

The spectral index (α) and the total observed flux are strongly anti-correlated, i.e., spectral hardening with increasing flux at most epochs for both blazars. That implies a "harder when brighter" trend in blazars, also found by other authors (Kapanadze et al. 2017, 2018; Hota et al. 2021; Wani et al. 2023). In addition, there is an anti-correlation between α and peak energy (E_{peak}), which is a consequence of a higher value of the peak energy when the spectrum is flatter. The correlations between the variation of β and total flux or E_{peak} are weak and in some epochs the sense changes such that they are weakly correlated or anti-correlated. In some HSP blazars the spectral curvature (β) and peak energy (E_{peak}) are anti-correlated, which has been explained by statistical acceleration of electrons (Massaro et al. 2006; Massaro, F. et al. 2008). Some authors (Hota et al. 2021; Khatoon et al. 2022) have shown that the observed flux and curvature are weakly correlated, which is consistent with our findings. On the other hand, α and β have an anti-correlation. Considering the log-parabolic particle energy distribution, Hota et al. (2021); Khatoon et al. (2022) have found negative relation, whereas Massaro et al. (2006); Massaro, F. et al. (2008) have found opposite nature. Hence, any clear trend in the $\alpha-\beta$ relationship is absent. It can be due to different physical mechanisms dominating the spectral variation at different times of observation.

From the comparison of theoretical modeling, we find that correlations of all four pairs of parameters generated in the cooling-dominated case of our theoretical model match well with the observations of Mrk 421 and 1ES 1959+650. Whereas, α and β exhibit a strong anti-correlation in Mrk 421, which is slightly better reproduced in the acceleration dominated case of the model. On the other hand, the general harder-when-brighter trend of the X-ray variation is much better reproduced in the cooling dominated scenario. Therefore, both cases with gradual acceleration and radiative cooling are partially able to reproduce observational results. That indicates the features of the model, e.g., the geometrical structure, physical parameters, and the emission mechanisms included are consistent with the observations. However, the trend in α and flux with E_{peak} could not show the observed trend for the case of gradual acceleration. That implies further details, in addition to an initial simple power-law energy distribution of emitting particles, such as more detailed acceleration mechanisms e.g., including stochastic acceleration and complex features in the geometric and emission properties of the jet, need to be considered to generate a more realistic X-ray emission model of the jet of HSP

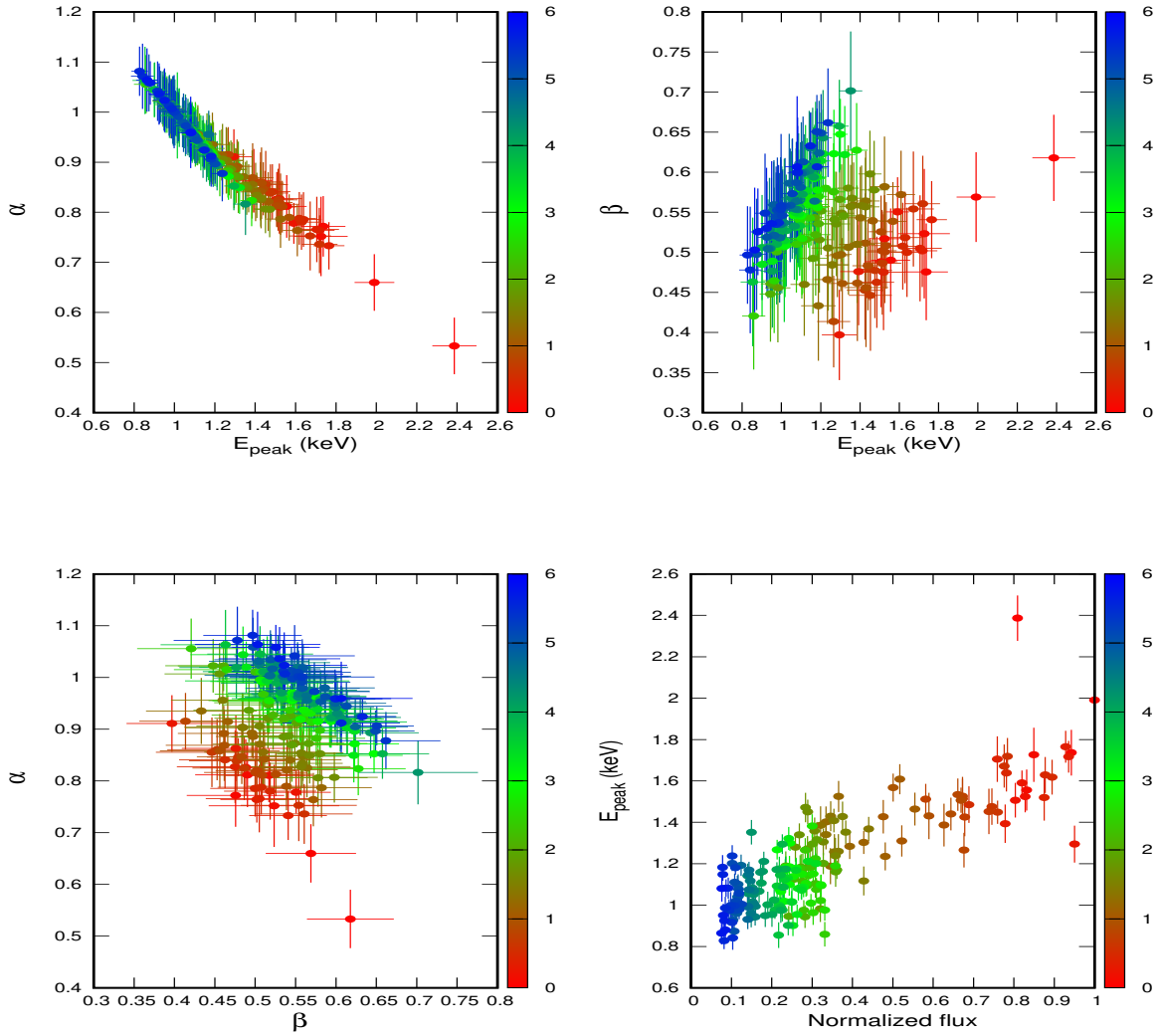

Fig. 11.— Correlation between the best-fit spectral parameters of the log-parabola model fit to the time-resolved simulated X-ray spectra at each snapshot of 5 ks interval for the case of radiative cooling only. The color bar indicates time evolution in days.

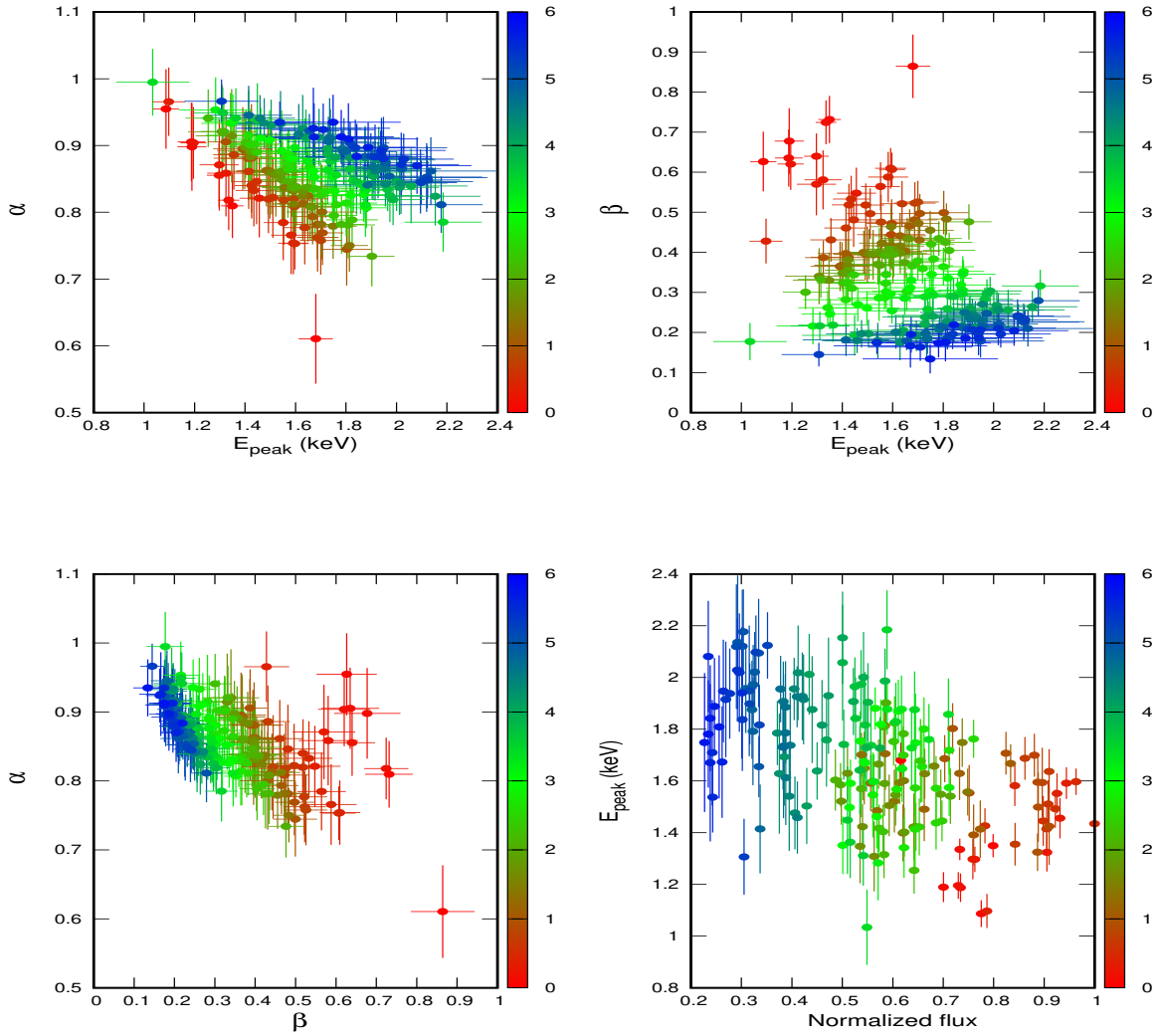

Fig. 12.— Correlation between the best-fit spectral parameters of the log-parabola model fit to the time-resolved simulated X-ray spectra at each snapshot of 5 ks interval for the case of gradual acceleration. The color bar indicates time evolution in days.

blazars.

5. Cross-Spectral Analysis of Hard and Soft X-ray Variations

The intra-day variation of HSP blazars at the X-ray band can show hard/soft lags, which are dependent on the underlying physical processes. Those are thought to be connected with energy dependent acceleration and cooling mechanisms in the jet (Zhang 2002). In order to study hard/soft X-ray time lags in more details, we carry out cross-spectrum analysis that provides Fourier frequency dependent time lags. If the X-ray fluctuations at different timescales contain different temporal properties, supposedly driven by different geometry or emission mechanisms, such that the strength of correlation and time lag are not the same at different timescales, that may be determined using the cross-spectrum. We aim to probe similar properties by a detailed cross-spectral analysis of multi-band X-ray light curves of some HSP blazars using *AstroSat* data.

5.1. Data

We have analysed SXT ($0.7-7$ keV) and LAXPC ($7-20$ keV) data of *AstroSat* for the blazars 1ES 1959+650 and Mrk 501 at different epochs which have data with long exposures and sufficient sampling. The light curves of SXT and LAXPC of those epochs are shown in Figures 13, 3. We divide the soft X-ray band into two energy ranges $(0.7-2)$ keV and $(2-7)$ keV to compute the cross-spectrum, i.e., the time lag between the X-ray bands in the frequency domain. We also check the cross-correlation and lags between those bands using the method discussed in Das & Chatterjee (2023) shown in Table 6.

Table 6: Cross-correlation coefficient (r_{max}) and centroid time lag (τ_{lag}) in hours of two HSP blazars between the inter-bands of X-ray $0.7-2$ keV, $2-7$ keV and $7-20$ keV represented as 1, 2, 3, respectively. Positive sign signifies hard lag and vice versa.

Source	Observation Date	r^{12}_{max}	τ^{12}_{lag}	r^{13}_{max}	τ^{13}_{lag}	r^{23}_{max}	τ^{23}_{lag}
1ES 1959+650	2016 November 3-7	0.96	$-0.93^{+0.82}_{-0.80}$	0.91	$-0.89^{+0.72}_{-0.67}$	0.94	$-0.11^{+0.85}_{-0.73}$
1ES 1959+650	2023 September 2-6	0.74	$-1.16^{+1.86}_{-1.31}$	0.72	$-0.04^{+1.89}_{-1.65}$	0.72	$0.34^{+1.81}_{-3.67}$
Mrk 501	2020 March 26-31	0.63	$-2.75^{+1.51}_{-1.12}$	0.39	$-4.78^{+3.65}_{-2.24}$	0.40	$0.38^{+2.57}_{-3.61}$
Mrk 501	2022 March 24-27	0.72	$-0.29^{+9.13}_{-4.64}$	0.75	$-3.20^{+4.79}_{-4.18}$	0.89	$-2.03^{+3.24}_{-2.48}$

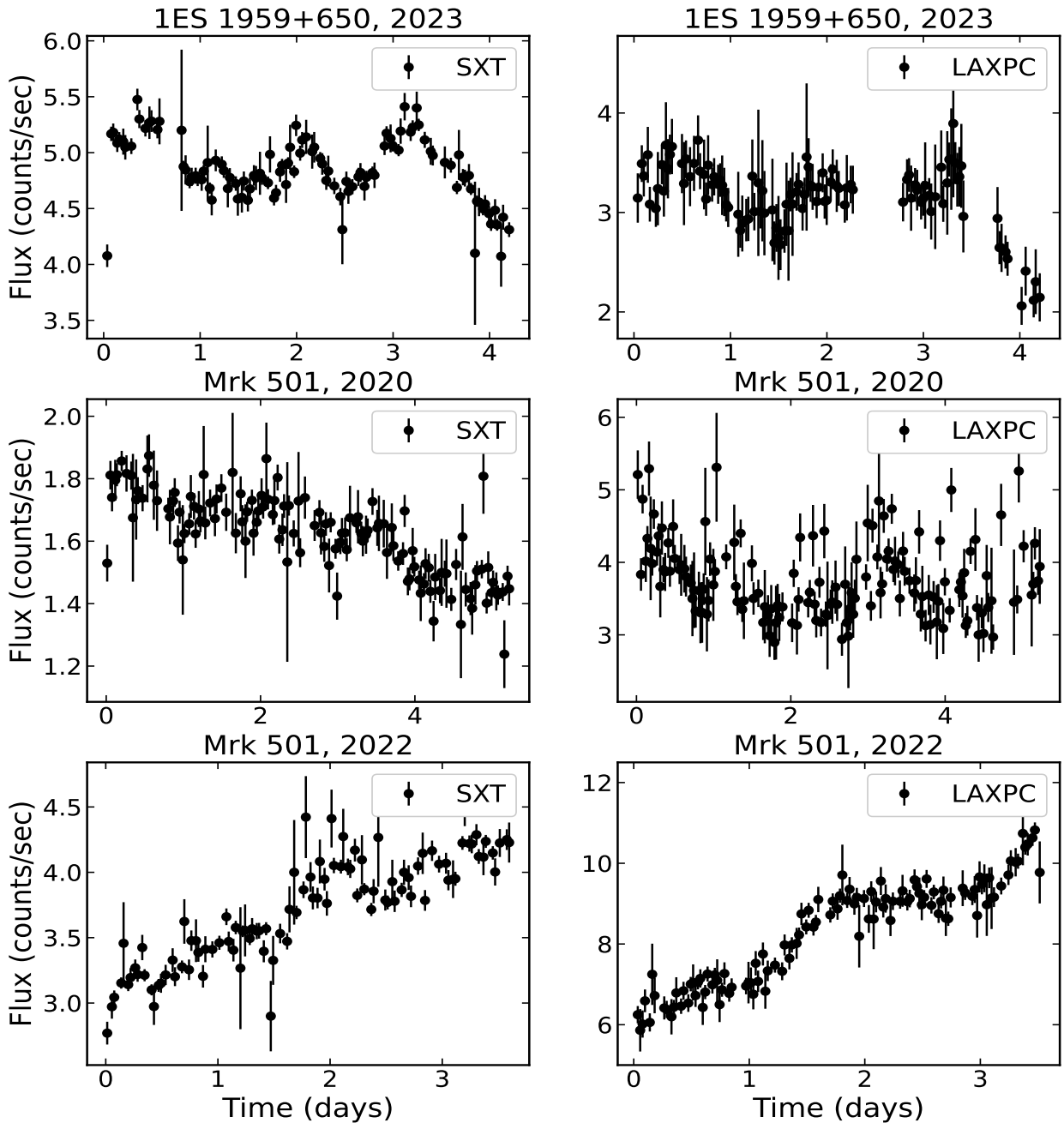

Fig. 13.— Soft ($0.7-7$ keV) and hard ($7-20$ keV) X-ray light curves of blazars 1ES 1959+650 and Mrk 501 from SXT and LAXPC instruments, respectively onboard *AstroSat* at multiple epochs (For epoch 2016 of 1ES 1959+650 see Figure 3).

5.2. Phase Spectrum

The phase spectrum measures the phase difference between a pair of light curves in Fourier frequency. The phase shifts ($\phi(f)$) are measured from the argument of the average cross-spectrum in every frequency bin. The time delay ($\tau(f)$) can be obtained by the ratio of the phase shift to 2π times the average frequency of the bin as follows,

$$\begin{aligned} \phi(f) &= Arg[\langle S^*(f)H(f)\rangle] \\ \tau(f) &= \phi(f)/(2\pi f) \end{aligned} \tag{14}$$

where $S(f)$ and $H(f)$ are the Fourier transforms of the two discrete uniformly sampled light curves. We used the methods described in Vaughan & Nowak (1997) and Nowak et al. (1999) to calculate the cross-spectrum. The phase lags remain bounded to [-π,π] and when a lag exceeds either of the boundaries it sharply changes sign.

The lag-spectrum of the two blazars 1ES 1959+650 and Mrk 501 between the energy bands $0.7-2$ keV, $2-7$ keV, and $7-20$ keV, calculated using the cross-spectral analysis method discussed above, are shown in Figures 14 and 15. The lower frequency lag at all epochs of both sources is consistent with the cross-correlation time delay (see Table 6). The obtained values of the cross-correlation lag vary corresponding to the pair of energy bands used, indicating the energy dependence of lags. The lag-spectra show that there exists a significant transition of lag from hard to soft or from soft to hard with increasing frequency in certain epochs. For example, the $2-7$ keV v/s $7-20$ keV spectrum of 1ES 1959+650 in 2023 shows a change of sign from positive to negative, i.e., hard to soft lag at $\sim 10^{-4}$ Hz, while the $0.7-2$ keV v/s $2-7$ keV and $2-7$ keV v/s $7-20$ keV spectra of Mrk 501 in 2020 shows a soft to hard lag transition at $\sim 5\times10^{-5}$ Hz (see left panels of Figures 14, 15). The sense of the time lag (positive/negative or hard/soft) indicates the dominance of the acceleration or cooling timescale of the emitting electrons assuming the X-ray emission has only synchrotron contribution. Lags at higher frequencies are consistent with zero due to the dominance of Poisson noise. We also calculate the coherence function for each pair of light curves, which are shown in the right panels of the respective Figures 14 and 15. It shows that the coherence is decreasing as frequency increases. The linearity of correlation within the energy bands drops rapidly due to non-linear counting noise of observations at shorter timescales.

6. Discussion

In this chapter, we investigate the hard and soft X-ray variations of two HSP blazars 1ES 1959+650 and Mrk 501 in Fourier domain. For that purpose, we have used *AstroSat* SXT and LAXPC data at multiple epochs. We perform cross-spectrum analysis between the energy bands $0.7-2$ keV, $2-7$ keV and $7-20$ keV to determine their time lags and coherence in terms of Fourier frequency.

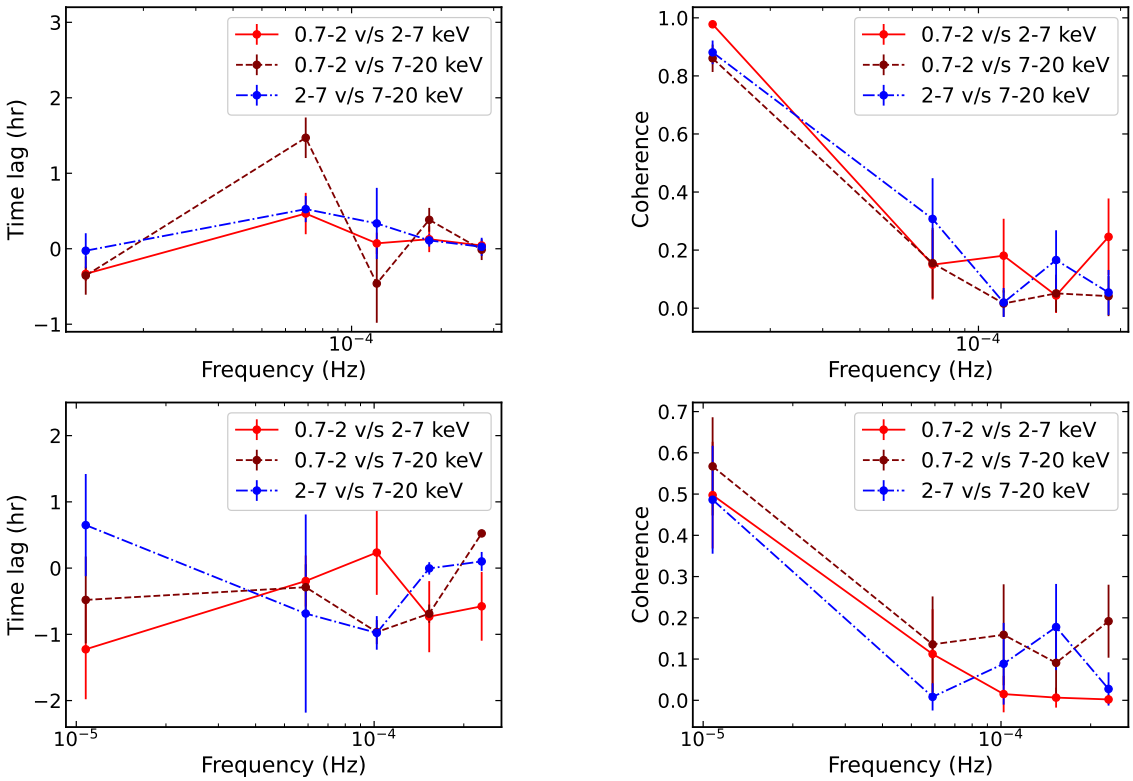

Fig. 14.— Frequency dependent time lag (left panel) and coherence (right panel) between X-ray energy bands $(0.7-2$ keV), $(2-7$ keV) and $(7-20$ keV) of blazar 1ES 1959+650 for the epochs of 2016 (upper panel) and 2023 (lower panel) from observations of SXT and LAXPC instruments onboard *AstroSat*.

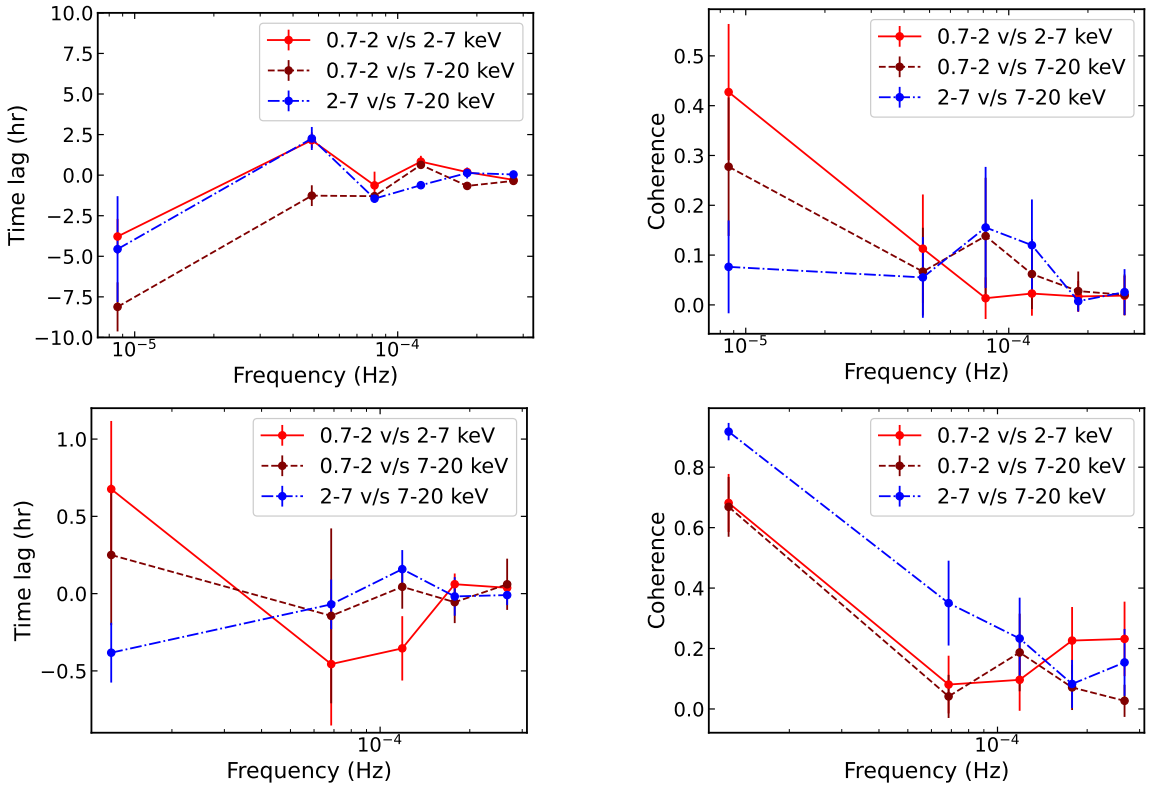

Fig. 15.— Frequency dependent time lag (left panel) and coherence (right panel) between X-ray energy bands ($0.7-2$ keV), ($2-7$ keV) and ($7-20$ keV) of blazar Mrk 501 for the epochs of 2020 (upper panel) and 2022 (lower panel) from observations of SXT and LAXPC instruments onboard *AstroSat*.

The lag-spectra show that the time lag between hard and soft X-ray light curves varies with frequency. At the lowest frequency or the longest timescale, the time lag is consistent with the cross-correlation delay. In some cases, the peak of the cross-correlation function is broad and the value of the delay has a large fractional uncertainty. As a result the sense of the delay is ambiguous. The time lag obtained from the cross-spectrum at the lowest frequency, in some cases, provides more unambiguous result. At the highest frequencies, the lag goes to zero with a change of sign in the middle frequencies in some cases. Synchrotron X-ray variability in the context of the leptonic model of blazar jet emission may be driven by several processes, e.g., injection of energetic electrons, variation of magnetic field in the emission region, cooling of the energetic particles, and change in the Doppler factor. Among those, fluctuating magnetic field may dominate the variability at the higher frequencies in the above cross-spectra, i.e., sub-day timescales. However, such variability may not generate any time lag and hence may cause a change in the lag value of the cross-spectrum from a positive or a negative value at lower frequencies. On the highest frequency end, the lag tends to zero because it is dominated by Poisson noise. Small fluctuations in the cross-spectrum about a lag value of zero close to the highest frequency end is generated by small-amplitude variability in the light curves. A sharp change in the value of the time lag is often caused by the effect of phase wrapping while a relatively slow change may be due to a change in the nature of the dominant physical process causing the variability, e.g., synchrotron cooling or gradual acceleration causing a hard or soft lag at longer timescales (lowest frequency end) to fluctuation of the magnetic field causing a lag consistent with zero.

7. Summary and Future Work

This work mainly focuses on the short-timescale, i.e., minutes to days scale, flux and spectral variability of blazars. Study of such short timescale variability is relatively uncommon because even the luminous blazars are not often sufficiently bright so that their light curves, when binned to such short time intervals, have significantly high signal to noise ratio. For this purpose, simultaneous hard and soft X-ray light curves of certain HSP blazars from *AstroSat*'s SXT and LAXPC instruments have been effective. In addition to those, we have also used (quasi)simultaneous observations in other wavebands e.g., GeV, and optical.

From multi-wavelength observations of Mrk 421, we have found shortest variability timescale at hard X-rays, longer at soft X-rays as well as optical-NIR bands. This confirms that X-rays in Mrk 421 are produced by synchrotron radiation of the highest energy electrons, in which faster variation with high variability amplitude is expected at shorter wavelength. Considering synchrotron cooling timescale for X-ray variability, we determine magnetic field ~ 0.5 Gauss and maximum Lorentz factor of emitting electrons $\sim 10^5$, which are consistent with values obtained from other kinds of studies, e.g. modeling of the broadband SED of those blazars. The GeV emission, on the other hand, is consistent with those generated due to IC scattering by relatively lower energy electrons such as those

producing the optical synchrotron emission. Those findings are consistent with the leptonic scenario of blazar emission.

We studied the X-ray variability of two HSP blazars, Mrk 421 and 1ES 1959+650, at multiple epochs of duration 40-400 ks during 2016-19. Cross-correlation results of the soft and hard X-ray light curves show that they are strongly correlated at a significance level of 95% or higher. We find both zero and non-zero (hard/soft) time lags within the X-ray bands. That indicates the electrons responsible for the observed X-ray variability are physically located in a compact region and undergo acceleration and cooling at approximately the same time. The hours-scale hard or soft lags indicate the domination of energy-dependent acceleration or cooling timescale of electrons, respectively. Using the hard and soft lags, we obtain a magnetic field ~ 0.1 Gauss, which is consistent with previous results. We also determine the acceleration parameter to be $\sim 10^4$, which may provide useful constraints on the elusive acceleration processes in the jet of blazars.

We also studied the $0.7 - 20$ keV X-ray spectra of Mrk 421 and 1ES 1959+650 from the above observations along with data from the Swift X-ray telescope. We find that the empirical log-parabola model provides a satisfactory fit to the spectra at all epochs. Through time-resolved spectroscopy of the above data, we find the variability of the best-fit spectral parameters at $\sim$hours timescale and their possible inter-relation. The correlation trends are related with physical processes and jet parameters. We discuss a theoretical model of jet emission by considering a multi-zone cylindrical geometrical structure, shock acceleration and radiative cooling mechanisms, which is able to reproduce the observed features of spectral variability. However, in addition to an initial simple power-law energy distribution of emitting particles, more detailed acceleration mechanisms, e.g., including stochastic acceleration and complex features in the geometric and emission properties of the jet, need to be considered to simulate more realistic emission variability in the jets of HSP blazars.

We have carried out cross-spectral analysis among X-ray light curves of HSP blazars at multiple bands to observe the variability properties at different timescales. We have obtained time lag as a function of Fourier frequencies, i.e., lag-spectrum for the blazars 1ES 1959+650 and Mrk 501, which show that the time lag varies with temporal frequencies. We find the time lag at the lowest frequency to be consistent with that found from cross-correlation analysis. At the highest frequencies, the time lag tends to zero due to the dominance of Poisson noise. In the middle frequencies, the time lag changes sense in some cases, which may be due to a change in the nature of the dominant physical process causing the variability, e.g., synchrotron cooling or gradual acceleration causing a soft or hard lag at lower frequencies (longer timescales) to fluctuation of the magnetic field at higher frequencies causing a lag consistent with zero.

Overall, we have confirmed and/or established a picture of the emission process in blazars. We found that the observed hours-days timescale flux and spectral variability of the blazars considered here are consistent with the following scenario. An emission region in the jet contains electrons, which are initially quiescent. Electrons located in successive sub-regions are accelerated, supposedly

by a moving shock wave, to a simple power-law energy distribution with a negative index ~ 2.5. The maximum Lorentz factor of the electrons is $\sim 10^5$, value of the magnetic field in the emission region is ~ 0.1 Gauss and it may contain smaller fluctuations. Those electrons start to cool radiatively by synchrotron and inverse-Compton processes and generate radio-γ-ray emission. The $0.7 - 20$ keV X-rays are produced by the synchrotron process, with no significant contribution from the IC peak of the SED, by the highest energy electrons such that the acceleration and cooling timescales are comparable. The exact timescales vary from one blazar to another and among different epochs. In some cases, the acceleration process may be longer such that it dominates the variability timescale. In those cases, an approximate estimate (0.01%-0.2%) of the energy gained in each step of scattering during acceleration may be obtained. This overall picture can provide useful constraints to future theories of jet launching and collimation and its interaction with the ISM and IGM.

List of Publications

Publications included in this thesis:

1. "*Short-Timescale Variability of the Blazar Mrk 421 from AstroSat and Simultaneous Multi-Wavelength Observations*", Chatterjee, R., **Das, S.**, et al., **2021**, JApA, 42, 80 (Special issue on 5 years of AstroSat), doi:10.1007/s12036-021-09709-3.

2. "*Correlated short time-scale hard-soft X-ray variability of the blazars Mrk 421 and 1ES 1959+650 using AstroSat"*, **Das, S.**, Chatterjee, R., **2023**, MNRAS, 524, 3797–3808, doi:10.1093/mnras/stad2131.

3. "*Sub-Day Timescale X-ray Spectral Variability of the TeV Blazars Mrk 421 and 1ES 1959+650"*, **Das, S.**, Chatterjee, R., **2024**, MNRAS, 539, 3582–3595, doi:10.1093/mnras/staf666.

Other Publication:

1. "*Multi-year characterisation of the broad-band emission from the intermittent extreme BL Lac 1ES 2344+514"*, H. Abe et al. (**MAGIC Collaboration** including **Das, S.**), **2024**, A&A 682, A114, doi:10.1051/0004-6361/202347845.

Successful Observing Proposals

1. *"AstroSat Observation of the TeV Blazar 1ES 1959+650 during A Very High Flaring State"*, **PI: Susmita Das**, awarded 100 ks in T05 cycle of **AstroSat**, ISRO.

2. *"Longlook Observations of Two TeV Blazars H 1426+428 and PG 1553+113"*, **PI: Susmita Das**, awarded 100 ks in A13 cycle of **AstroSat**, ISRO.

3. *"Characterization of the extreme nature of the blazar TXS0210+515"*, PI: Pratik Majumdar, **Co-I: Susmita Das**, awarded 100 ks in A11 cycle of **AstroSat**, ISRO.

4. *"Spectral Energy Distribution and Time Variability of the TeV Blazar 1ES 2344+514"*, PI: Ritaban Chatterjee, **Co-I: Susmita Das**, awarded 100 ks in A10 cycle of **AstroSat**, ISRO.

Contributed Presentations

1. **Oral:** *"Sub-Day Timescale X-ray Spectral Variability of the TeV Blazars Mrk 421 and 1ES 1959+650"*, "Conference On Blazar and Restless AGN (COBRA)", 22-26th July, 2024, Presidency University, Kolkata.

2. **Poster:** *"X-ray Spectral Variability Studies of High Synchrotron Peaked Blazars using AstroSat"*, 41st meeting of Astronomical Society of India (ASI), 1-5th March, 2023, IIT Indore, Indore.

3. **Oral:** *"Acceleration and Radiative Cooling Timescale in the Jets of Blazars from AstroSat Observations"*, International Astronomical Union (IAU) Symposium 375, "The Multimessenger Chakra of Blazar Jets", 5-9th December, 2022, Kathmandu, Nepal.

4. **Poster:** *"Temporal and Spectral Studies of Two Blazars at X-ray Energies using AstroSat"*, Young Astronomer's Meet (YAM) 2022, 9-13th November, 2022, ARIES, Nainital.

5. **Oral:** *"Acceleration and Radiative Cooling Timescale in the Jets of Blazars from AstroSat Observations"*, "Celebration of 7 years of AstroSat", 28-29th September, 2022, ISRO, Bengaluru.

6. **Oral:** *"Acceleration and Radiative Cooling Timescale in the Jets of Blazars from AstroSat Observations"*, IUCAA sponsored 4th National Conference on "High Energy Emission from Active Galactic Nuclei", 12-14th August, 2022, Farook College, Kozhikode, Kerala.

7. **Poster (virtual):** *"Relation between Hard and Soft X-ray Emission in Two TeV blazars using AstroSat"*, 40th Annual meeting of Astronomical Society of India (ASI), 25-29th March, 2022.

8. **Flash poster (virtual):** *"Short-Timescale Variability of the Blazar Mrk 421 from AstroSat and Simultaneous Multi-Wavelength Observations"*, 21st National Space Science Symposium (NSSS), IISER Kolkata, 31st January - 4th February, 2022.

9. **Poster (virtual):** *"Estimating Physical Parameters of the Jet from Short-timescale Multi-wavelength Variability of the Blazar Mrk 421"*, 39th Annual meeting of Astronomical Society of India (ASI), 18-23th February 2021.

10. **Poster (virtual):** *"Short-Timescale Variability of the Blazar Mrk 421 from AstroSat and Simultaneous Multi-Wavelength Observations"*, International conference on 5 years of AstroSat, ISRO, 19-21st January, 2021.

Acknowledgment

Firstly, I would like to express my sincere gratitude to my supervisor, Dr. Ritaban Chatterjee, for his complete support, help and valuable guidance. I would like to thank the Research Advisory Committee and PhD Committee members for their advice in improving my thesis work. I am deeply grateful to all of my colleagues, co-authors, and friends for their continued support and help throughout my PhD journey. I thank Jayashree Roy, Sunil Chandra, Ritesh Ghosh, Savithri Ezhikode, Gulab Dewangan, and Ranjeev Misra for useful discussion regarding AstroSat data analysis. I am thankful to Kaustav Mitra, Arit Bala and Agniva Roychowdhury for discussion related to blazar emission model and timing analyses. I would like to thank IUCAA for their hospitality and for providing access to their facilities during my visit. I acknowledge financial support from ISRO under the AstroSat data utilization program and the ANRF SURE grant.

REFERENCES

Abdo, A. A., Ackermann, M., Agudo, I., et al. 2010, ApJ, 716, 30, doi: 10.1088/0004-637X/716/1/30

Abdo, A. A., Ackermann, M., Ajello, M., et al. 2011, ApJ, 736, 131, doi: 10.1088/0004-637X/736/2/131

Ackermann, M., Anantua, R., Asano, K., et al. 2016, ApJ, 824, L20, doi: 10.3847/2041-8205/824/2/L20

Antonucci, R. R. J., & Miller, J. S. 1985, ApJ, 297, 621, doi: 10.1086/163559

Banerjee, B., Joshi, M., Majumdar, P., et al. 2019, MNRAS, 487, 845, doi: 10.1093/mnras/stz1292

Barat, S., Chatterjee, R., & Mitra, K. 2022, MNRAS, 515, 1655, doi: 10.1093/mnras/stac1852

Baring, M. G., Böttcher, M., & Summerlin, E. J. 2017, MNRAS, 464, 4875, doi: 10.1093/mnras/stw2344

Baring, M. G., W. Ogilvie, C. Ellison, & Forsyth, R. J. 1997, ApJ, 476, 889, doi: 10.1086/303645

Blandford, R., & Eichler, D. 1987, Phys. Rep., 154, 1, doi: 10.1016/0370-1573(87)90134-7

Blandford, R. D., & Rees, M. J. 1974, MNRAS, 169, 395, doi: 10.1093/mnras/169.3.395

Blinov, D., Pavlidou, V., Papadakis, I. E., et al. 2016, MNRAS, 457, 2252, doi: 10.1093/mnras/stw158

Bloom, S. D., & Marscher, A. P. 1996, ApJ, 461, 657, doi: 10.1086/177092

Bottacini, E., Böttcher, M., Pian, E., & Collmar, W. 2016, ApJ, 832, 17, doi: 10.3847/0004-637X/832/1/17

Böttcher, M. 2019, Galaxies, 7, 20, doi: 10.3390/galaxies7010020

Böttcher, M., & Dermer, C. D. 2010, ApJ, 711, 445, doi: 10.1088/0004-637X/711/1/445

Bregman, J. N., Lebofsky, M. J., Aller, M. F., et al. 1981, Nature, 293, 714, doi: 10.1038/293714a0

Chandra, S., Boettcher, M., Goswami, P., et al. 2021, ApJ, 918, 67, doi: 10.3847/1538-4357/ac01d1

Chatterjee, R., Roychowdhury, A., Chandra, S., & Sinha, A. 2018, ApJ, 859, L21, doi: 10.3847/2041-8213/aac48a

Chatterjee, R., Jorstad, S. G., Marscher, A. P., et al. 2008, ApJ, 689, 79, doi: 10.1086/592598

Chatterjee, R., Bailyn, C. D., Bonning, E. W., et al. 2012, ApJ, 749, 191, doi: 10.1088/0004-637X/749/2/191

Chen, L. 2014, ApJ, 788, 179, doi: 10.1088/0004-637X/788/2/179

Chiaberge, M., & Ghisellini, G. 1999, MNRAS, 306, 551, doi: 10.1046/j.1365-8711.1999.02538.x

Das, S., & Chatterjee, R. 2023, MNRAS, 524, 3797, doi: 10.1093/mnras/stad2131

Edelson, R. A., & Krolik, J. H. 1988, ApJ, 333, 646, doi: 10.1086/166773

Evans, P. A., Beardmore, A. P., Page, K. L., et al. 2009, MNRAS, 397, 1177, doi: 10.1111/j.1365-2966.2009.14913.x

Franceschini, A., Vercellone, S., & Fabian, A. C. 1998, MNRAS, 297, 817, doi: 10.1046/j.1365-8711.1998.01534.x

Gaskell, C. M. 2009, New A Rev., 53, 140, doi: 10.1016/j.newar.2009.09.006

Ghisellini, G., Celotti, A., Fossati, G., Maraschi, L., & Comastri, A. 1998, MNRAS, 301, 451, doi: 10.1046/j.1365-8711.1998.02032.x

Ghisellini, G., Padovani, P., Celotti, A., & Maraschi, L. 1993, ApJ, 407, 65, doi: 10.1086/172493

Ghisellini, G., Tavecchio, F., Foschini, L., & Ghirlanda, G. 2011, MNRAS, 414, 2674, doi: 10.1111/j.1365-2966.2011.18578.x

Giommi, P., Polenta, G., Lähteenmäki, A., et al. 2012, A&A, 541, A160, doi: 10.1051/0004-6361/201117825

Giommi, P., Perri, M., Capalbi, M., et al. 2021, MNRAS, 507, 5690, doi: 10.1093/mnras/stab2425

Graff, P. B., Georganopoulos, M., Perlman, E. S., & Kazanas, D. 2008, ApJ, 689, 68, doi: 10.1086/592427

Hota, J., Shah, Z., Khatoon, R., et al. 2021, MNRAS, 508, 5921, doi: 10.1093/mnras/stab2903

Inoue, S., & Takahara, F. 1996, ApJ, 463, 555, doi: 10.1086/177270

Joshi, M., & Böttcher, M. 2011, ApJ, 727, 21, doi: 10.1088/0004-637X/727/1/21

Kalberla, P. M. W., Burton, W. B., Hartmann, D., et al. 2005, A&A, 440, 775, doi: 10.1051/0004-6361:20041864

Kapanadze, B., Dorner, D., Romano, P., et al. 2017, ApJ, 848, 103, doi: 10.3847/1538-4357/aa8ea6

Kapanadze, B., Dorner, D., Vercellone, S., et al. 2018, ApJS, 238, 13, doi: 10.3847/1538-4365/aad8b5

Kazanas, D., Titarchuk, L. G., & Hua, X.-M. 1998, ApJ, 493, 708, doi: 10.1086/305131

Kellermann, K. I., Sramek, R., Schmidt, M., Shaffer, D. B., & Green, R. 1989, AJ, 98, 1195, doi: 10.1086/115207

Khatoon, R., Shah, Z., Hota, J., et al. 2022, MNRAS, 515, 3749, doi: 10.1093/mnras/stac1964

Kirk, J. G., Rieger, F. M., & Mastichiadis, A. 1998, A&A, 333, 452. https://arxiv.org/abs/astro-ph/9801265

Kundu, A., Chatterjee, R., Mitra, K., & Mondal, S. 2022, MNRAS, 510, 3688, doi: 10.1093/mnras/stab3750

Kusunose, M., Takahara, F., & Li, H. 2000, ApJ, 536, 299, doi: 10.1086/308928

Lawrence, A., Watson, M. G., Pounds, K. A., & Elvis, M. 1987, Nature, 325, 694, doi: 10.1038/325694a0

Liodakis, I., Marscher, A. P., Agudo, I., et al. 2022, Nature, 611, 677, doi: 10.1038/s41586-022-05338-0

Lister, M. L., Aller, M. F., Aller, H. D., et al. 2018, ApJS, 234, 12, doi: 10.3847/1538-4365/aa9c44

Liu, R.-Y., Xue, R., Wang, Z.-R., Tan, H.-B., & Böttcher, M. 2023, MNRAS, 526, 5054, doi: 10.1093/mnras/stad2911

Markowitz, A. G., Nalewajko, K., Bhatta, G., et al. 2022, MNRAS, 513, 1662, doi: 10.1093/mnras/stac917

Marscher, A. 2016, Galaxies, 4, 37, doi: 10.3390/galaxies4040037

Marscher, A. P. 1998, in Astronomical Society of the Pacific Conference Series, Vol. 144, IAU Colloq. 164: Radio Emission from Galactic and Extragalactic Compact Sources, ed. J. A. Zensus, G. B. Taylor, & J. M. Wrobel, 25

Marscher, A. P. 2014, ApJ, 780, 87, doi: 10.1088/0004-637X/780/1/87

Massaro, E., Tramacere, A., Perri, M., Giommi, P., & Tosti, G. 2006, A&A, 448, 861, doi: 10.1051/0004-6361:20053644

Massaro, F., Tramacere, A., Cavaliere, A., Perri, M., & Giommi, P. 2008, A&A, 478, 395, doi: 10.1051/0004-6361:20078639

McNamara, B. R., & Nulsen, P. E. J. 2007, ARA&A, 45, 117, doi: 10.1146/annurev.astro.45.051806.110625

Mücke, A., & Protheroe, R. J. 2001, Astroparticle Physics, 15, 121, doi: 10.1016/S0927-6505(00)00141-9

Mücke, A., Protheroe, R. J., Engel, R., Rachen, J. P., & Stanev, T. 2003, Astroparticle Physics, 18, 593, doi: 10.1016/S0927-6505(02)00185-8

Netzer, H., & Laor, A. 1993, ApJ, 404, L51, doi: 10.1086/186741

Nowak, M. A., Vaughan, B. A., Wilms, J., Dove, J. B., & Begelman, M. C. 1999, ApJ, 510, 874, doi: 10.1086/306610

Padovani, P., & Giommi, P. 1995, MNRAS, 277, 1477, doi: 10.1093/mnras/277.4.1477

Padovani, P., Alexander, D. M., Assef, R. J., et al. 2017, A&A Rev., 25, 2, doi: 10.1007/s00159-017-0102-9

Peterson, B. M., Wanders, I., Horne, K., et al. 1998, PASP, 110, 660, doi: 10.1086/316177

Punch, M., Akerlof, C. W., Cawley, M. F., et al. 1992, Nature, 358, 477, doi: 10.1038/358477a0

Rajput, B., Stalin, C. S., & Rakshit, S. 2020, A&A, 634, A80, doi: 10.1051/0004-6361/201936769

Rani, B., Krichbaum, T. P., Fuhrmann, L., et al. 2013, A&A, 552, A11, doi: 10.1051/0004-6361/201321058

Ravasio, M., Tagliaferri, G., Ghisellini, G., & Tavecchio, F. 2004, A&A, 424, 841, doi: 10.1051/0004-6361:20034545

Richstone, D., Ajhar, E. A., Bender, R., et al. 1998, Nature, 385, A14, doi: 10.48550/arXiv.astro-ph/9810378

Roy, N., Chatterjee, R., Joshi, M., & Ghosh, A. 2019, MNRAS, 482, 743, doi: 10.1093/mnras/sty2748

Rybicki, G. B., & Lightman, A. P. 1979, Radiative processes in astrophysics

Saito, S., Stawarz, Ł., Tanaka, Y. T., et al. 2013, ApJ, 766, L11, doi: 10.1088/2041-8205/766/1/L11

Salpeter, E. E. 1964, ApJ, 140, 796, doi: 10.1086/147973

Shah, Z., Ezhikode, S. H., Misra, R., & Rajalakshmi, T. R. 2021, MNRAS, 504, 5485, doi: 10.1093/mnras/stab1244

Shakura, N. I., & Sunyaev, R. A. 1973, A&A, 24, 337

Sikora, M., Begelman, M. C., & Rees, M. J. 1994, ApJ, 421, 153, doi: 10.1086/173633

Singh, K. P., Stewart, G. C., Chandra, S., et al. 2016, in Society of Photo-Optical Instrumentation Engineers (SPIE) Conference Series, Vol. 9905, Space Telescopes and Instrumentation 2016: Ultraviolet to Gamma Ray, ed. J.-W. A. den Herder, T. Takahashi, & M. Bautz, 99051E, doi: 10.1117/12.2235309

Sun, M., Grier, C. J., & Peterson, B. M. 2018, PyCCF: Python Cross Correlation Function for reverberation mapping studies, Astrophysics Source Code Library, record ascl:1805.032. http://ascl.net/1805.032

Timmer, J., & Koenig, M. 1995, A&A, 300, 707

Urry, C. M., & Padovani, P. 1995, PASP, 107, 803, doi: 10.1086/133630

Vaughan, B. A., & Nowak, M. A. 1997, ApJ, 474, L43, doi: 10.1086/310430

Wani, K., Gaur, H., & Patil, M. K. 2023, ApJ, 951, 94, doi: 10.3847/1538-4357/acd186

Wierzcholska, A., Zacharias, M., Jankowsky, F., Wagner, S., & H. E. S. S. Collaboration. 2019, Galaxies, 7, 21, doi: 10.3390/galaxies7010021

Yadav, J. S., Agrawal, P. C., Antia, H. M., et al. 2016, in Society of Photo-Optical Instrumentation Engineers (SPIE) Conference Series, Vol. 9905, Space Telescopes and Instrumentation 2016: Ultraviolet to Gamma Ray, ed. J.-W. A. den Herder, T. Takahashi, & M. Bautz, 99051D, doi: 10.1117/12.2231857

Zel'dovich, Y. B., & Novikov, I. D. 1964, Soviet Physics Doklady, 9, 246

Zhang, Y. H. 2002, MNRAS, 337, 609, doi: 10.1046/j.1365-8711.2002.05958.x

Zhang, Y. H., Treves, A., Maraschi, L., Bai, J. M., & Liu, F. K. 2006, ApJ, 637, 699, doi: 10.1086/498498

Zhang, Y. H., Treves, A., Celotti, A., et al. 2002, ApJ, 572, 762, doi: 10.1086/340349

This preprint was prepared with the AAS LaTeX macros v5.2.